



## Review

## State of the art satellite and airborne marine oil spill remote sensing: Application to the BP Deepwater Horizon oil spill

Ira Leifer <sup>a,\*</sup>, William J. Lehr <sup>b</sup>, Debra Simecek-Beatty <sup>b</sup>, Eliza Bradley <sup>c</sup>, Roger Clark <sup>d</sup>, Philip Dennison <sup>e</sup>, Yongxiang Hu <sup>f</sup>, Scott Matheson <sup>e</sup>, Cathleen E. Jones <sup>g</sup>, Benjamin Holt <sup>g</sup>, Molly Reif <sup>h</sup>, Dar A. Roberts <sup>c</sup>, Jan Svejkovsky <sup>i</sup>, Gregg Swayze <sup>d</sup>, Jennifer Wozencraft <sup>h</sup>

<sup>a</sup> Marine Science Institute, University of California, Santa Barbara, CA, United States

<sup>b</sup> NOAA Office of Response and Restoration, Seattle, WA, United States

<sup>c</sup> Geography Department, University of California, Santa Barbara, CA, United States

<sup>d</sup> US Geological Survey, Denver, United States

<sup>e</sup> Department of Geography and Center for Natural and Technological Hazards, University of Utah, Salt Lake City, UT, United States

<sup>f</sup> NASA Langley Research Center, Hampton, VA, United States

<sup>g</sup> Jet Propulsion Laboratory, California Institute of Technology, Pasadena, CA, United States

<sup>h</sup> US Army Corp of Engineers, Kiln MS, United States

<sup>i</sup> Ocean Imaging Corporation, Solana Beach, CA, United States

## ARTICLE INFO

## Article history:

Received 21 July 2011

Received in revised form 20 March 2012

Accepted 24 March 2012

Available online xxxx

## Keywords:

Oil spill

Deepwater Horizon

Remote sensing

Lidar

Near infrared

Thermal infrared

Satellite

Airborne remote sensing

Synthetic aperture radar

MODIS

Hyperspectral

Multispectral

Expert system

False positives

Technology readiness

Operational readiness

Visible spectrum

Oil water emulsions

Spill response

AVIRIS

Synthetic aperture radar

UAVSAR

Fire

CALIPSO

Oil slick thickness

Laser fluorescence

## ABSTRACT

The vast and persistent Deepwater Horizon (DWH) spill challenged response capabilities, which required accurate, quantitative oil assessment at synoptic and operational scales. Although experienced observers are a spill response's mainstay, few trained observers and confounding factors including weather, oil emulsification, and scene illumination geometry present challenges. DWH spill and impact monitoring was aided by extensive airborne and spaceborne passive and active remote sensing.

Oil slick thickness and oil-to-water emulsion ratios are key spill response parameters for containment/cleanup and were derived quantitatively for thick ( $>0.1$  mm) slicks from AVIRIS (Airborne Visible/Infrared Imaging Spectrometer) data using a spectral library approach based on the shape and depth of near infrared spectral absorption features. MODIS (Moderate Resolution Imaging Spectroradiometer) satellite, visible-spectrum broadband data of surface-slick modulation of sunglint reflection allowed extrapolation to the total slick. A multispectral expert system used a neural network approach to provide Rapid Response thickness class maps.

Airborne and satellite synthetic aperture radar (SAR) provides synoptic data under all-sky conditions; however, SAR generally cannot discriminate thick ( $>100$   $\mu$ m) oil slicks from thin sheens (to 0.1  $\mu$ m). The UAVSAR's (Uninhabited Aerial Vehicle SAR) significantly greater signal-to-noise ratio and finer spatial resolution allowed successful pattern discrimination related to a combination of oil slick thickness, fractional surface coverage, and emulsification.

In situ burning and smoke plumes were studied with AVIRIS and corroborated spaceborne CALIPSO (Cloud Aerosol Lidar and Infrared Pathfinder Satellite Observation) observations of combustion aerosols. CALIPSO and bathymetry lidar data documented shallow subsurface oil, although ancillary data were required for confirmation.

Airborne hyperspectral, thermal infrared data have nighttime and overcast collection advantages and were collected as well as MODIS thermal data. However, interpretation challenges and a lack of Rapid Response Products prevented significant use. Rapid Response Products were key to response utilization—data needs are time critical; thus, a high technological readiness level is critical to operational use of remote sensing products. DWH's experience demonstrated that development and operationalization of new spill response remote sensing tools must precede the next major oil spill.

© 2012 Elsevier Inc. All rights reserved.

\* Corresponding author.

E-mail address: [Ira.Leifer@bubbleology.com](mailto:Ira.Leifer@bubbleology.com) (I. Leifer).

## Report Documentation Page

*Form Approved  
OMB No. 0704-0188*

Public reporting burden for the collection of information is estimated to average 1 hour per response, including the time for reviewing instructions, searching existing data sources, gathering and maintaining the data needed, and completing and reviewing the collection of information. Send comments regarding this burden estimate or any other aspect of this collection of information, including suggestions for reducing this burden, to Washington Headquarters Services, Directorate for Information Operations and Reports, 1215 Jefferson Davis Highway, Suite 1204, Arlington VA 22202-4302. Respondents should be aware that notwithstanding any other provision of law, no person shall be subject to a penalty for failing to comply with a collection of information if it does not display a currently valid OMB control number.

|   |                                    |   |                                  |                                 |
|---|------------------------------------|---|----------------------------------|---------------------------------|
| 1. REPORT DATE<br><b>2012</b>   | 2. REPORT TYPE                     | 3. DATES COVERED<br><b>00-00-2012 to 00-00-2012</b>       |                                  |                                 |
| 4. TITLE AND SUBTITLE<br><b>Remote Sensing of Environment</b>   |                                    | 5a. CONTRACT NUMBER                                       |                                  |                                 |
|   |                                    | 5b. GRANT NUMBER  |                                  |                                 |
|   |                                    | 5c. PROGRAM ELEMENT NUMBER                                |                                  |                                 |
| 6. AUTHOR(S)  |                                    | 5d. PROJECT NUMBER  |                                  |                                 |
|   |                                    | 5e. TASK NUMBER   |                                  |                                 |
|   |                                    | 5f. WORK UNIT NUMBER                                      |                                  |                                 |
| 7. PERFORMING ORGANIZATION NAME(S) AND ADDRESS(ES)<br><b>US Geological Survey, Federal Ave, Denver, CO, 80225</b> |                                    | 8. PERFORMING ORGANIZATION REPORT NUMBER                  |                                  |                                 |
| 9. SPONSORING/MONITORING AGENCY NAME(S) AND ADDRESS(ES)   |                                    | 10. SPONSOR/MONITOR'S ACRONYM(S)                          |                                  |                                 |
|   |                                    | 11. SPONSOR/MONITOR'S REPORT NUMBER(S)                    |                                  |                                 |
| 12. DISTRIBUTION/AVAILABILITY STATEMENT<br><b>Approved for public release; distribution unlimited</b>             |                                    |   |                                  |                                 |
| 13. SUPPLEMENTARY NOTES   |                                    |   |                                  |                                 |
| 14. ABSTRACT  |                                    |   |                                  |                                 |
| 15. SUBJECT TERMS   |                                    |   |                                  |                                 |
| 16. SECURITY CLASSIFICATION OF:   |                                    | 17. LIMITATION OF ABSTRACT<br><b>Same as Report (SAR)</b> | 18. NUMBER OF PAGES<br><b>26</b> | 19a. NAME OF RESPONSIBLE PERSON |
| a. REPORT<br><b>unclassified</b>  | b. ABSTRACT<br><b>unclassified</b> |   |                                  |                                 |

## Contents

|  |     |
|--|-----|
| 1. Introduction . . . . .  | 186 |
| 1.1. Overview . . . . .  | 186 |
| 1.2. Background: oil slick science . . . . .                                     | 187 |
| 1.2.1. Marine oil sources . . . . .  | 187 |
| 1.2.2. Oil slick processes . . . . .   | 187 |
| 1.2.3. Oil spill response . . . . .  | 187 |
| 1.2.4. Oil slick remote sensing for oil spill response . . . . .                 | 188 |
| 1.3. Oil slick remote sensing of the DWH . . . . .                               | 188 |
| 2. Passive remote sensing of oil slicks . . . . .                                | 189 |
| 2.1. Background: oil slick spectroscopy . . . . .                                | 189 |
| 2.1.1. Visible appearance of oil slicks . . . . .                                | 189 |
| 2.1.2. Visible spectrum oil slick assessment . . . . .                           | 190 |
| 2.1.3. Visible spectrum oil slick appearance: underlying spectroscopy . . . . .  | 191 |
| 2.1.4. Near infrared oil slick appearance: underlying spectroscopy . . . . .     | 191 |
| 2.1.5. Thermal infrared oil slick appearance (emissivity) . . . . .              | 193 |
| 2.2. Passive oil slick remote sensing . . . . .                                  | 194 |
| 2.2.1. Multispectral (visible and thermal) expert system . . . . .               | 194 |
| 2.2.2. Quantitative oil slick imaging spectroscopy . . . . .                     | 194 |
| 2.2.3. Satellite visible oil slick remote sensing . . . . .                      | 194 |
| 2.2.4. Satellite thermal infrared oil slick remote sensing . . . . .             | 195 |
| 2.3. Oil slick passive remote sensing of DWH . . . . .                           | 195 |
| 2.3.1. Airborne oil slick remote sensing data collection . . . . .               | 195 |
| 2.3.2. Multispectral oil slick thickness classification of DWH . . . . .         | 196 |
| 2.3.3. Hyperspectral quantitative oil slick mapping of the DWH . . . . .         | 197 |
| 2.3.4. Airborne thermal infrared oil slick mapping of the DWH . . . . .          | 197 |
| 2.3.5. Satellite oil slick remote sensing of the DWH . . . . .                   | 198 |
| 3. Active oil slick remote sensing . . . . .                                     | 198 |
| 3.1. Background: active oil slick remote sensing . . . . .                       | 198 |
| 3.1.1. Synthetic aperture radar oil slick observations . . . . .                 | 198 |
| 3.1.2. Airborne and spaceborne synthetic aperture radar . . . . .                | 199 |
| 3.1.3. Laser oil slick remote sensing . . . . .                                  | 199 |
| 3.2. Active remote sensing of the DWH . . . . .                                  | 200 |
| 3.2.1. Airborne Synthetic aperture radar remote sensing of the DWH . . . . .     | 200 |
| 3.2.2. Satellite synthetic aperture radar remote sensing of the DWH . . . . .    | 201 |
| 3.2.3. Airborne and spaceborne laser remote sensing of the DWH . . . . .         | 201 |
| 4. Oil spill impacts . . . . .   | 201 |
| 4.1. Background: oil slick impact remote sensing . . . . .                       | 201 |
| 4.1.1. Vegetation and ecosystem impacts . . . . .                                | 201 |
| 4.1.2. Fire and oil spills . . . . .   | 202 |
| 4.1.3. Oil spill fire aerosols . . . . .   | 202 |
| 4.1.4. Oil slick volatiles . . . . .   | 202 |
| 4.2. Oil slick ecosystem impact remote sensing of the DWH . . . . .              | 204 |
| 4.2.1. In situ burning and well flaring . . . . .                                | 204 |
| 4.2.2. Oil slick trace gases remote sensing of the DWH . . . . .                 | 205 |
| 4.3. Vegetation and ecosystem impacts remote sensing of the DWH . . . . .        | 205 |
| 5. Discussion . . . . .  | 205 |
| 5.1. Oil slick remote sensing . . . . .  | 205 |
| 5.1.1. Passive airborne oil slick remote sensing . . . . .                       | 205 |
| 5.1.2. Passive satellite oil slick remote sensing . . . . .                      | 206 |
| 5.1.3. Active satellite and airborne oil slick remote sensing . . . . .          | 206 |
| 5.2. Applications of quantitative oil slick thickness mapping . . . . .          | 206 |
| 5.3. Real world application of remote sensing technology to oil slicks . . . . . | 206 |
| 6. Conclusions . . . . .   | 207 |
| Acknowledgments . . . . .  | 207 |
| References . . . . .   | 207 |

## 1. Introduction

## 1.1. Overview

Marine petroleum affects the environment, economy, and quality of life for coastal inhabitants leading to concerns that include resource exploration, recovery, transportation, and resultant oil spill contingency planning, mitigation, and remediation (Jensen et al., 1990). Traditionally, remote sensing has played a secondary support role in oil spill response and monitoring. However, recent technological

advancements and sensor availability have enabled a more important role for remote sensing. During the *Deepwater Horizon* (DWH) spill, several remote sensing technologies rapidly moved up the technological readiness scale (Ramirez-Marquez & Sauser, 2009), propelled by the spill's scale and urgency.

In this review, we summarize and discuss the role of remote sensing technologies used in the DWH response with varying degrees of effectiveness. This paper has five sections: 1) oil spill processes relevant to oil spill response and remote sensing interpretation, 2) passive oil-spectroscopy and remote sensing, 3) active oil remote sensing, 4) remote

sensing oil spill impacts, and 5) a final discussion. Each section presents background, available remote sensing tools, and their DWH application, with discussion of both airborne and orbital sensors.

## 1.2. Background: oil slick science

### 1.2.1. Marine oil sources

Annually, on average 1,300,000 t of oil entered the oceans during the 1990s with tanker vessel spills accounting for 100,000 t, run-off 140,000 t, and pipeline leaks just 12,000 t (NRC, 2003). Aside from natural seeps, which contribute an estimated 600,000 t or ~45% of total emissions, other important sources include vessel operational discharges (NRC, 2003). Oil spills impacting coastal waters are occurrence with a cumulative total of 447 U.S. oil and chemical spills reported from 1992 to 1999, with 50 between Oct. 1998 and Oct. 1999 (NRC, 2003). Tanker spills generally have decreased in volume with only 100 t spilled in 2009, whereas, at least 138,000 t were spilled each year in the 1970s. Large spills like the Prestige in 2002 (63,000 t) still occur. In contrast, spills resulting from sabotage and pipeline ruptures are increasing due in part to aging pipeline networks and infrastructure expanding into ever deeper waters (Jernelöv, 2010).

Although natural seeps are estimated as the largest marine oil source, few fluxes have been measured. Annually, North American seeps emit an estimated 160,000 t of oil with California seeps contributing 20,000 t of oil, ~12% of the North American total emissions (NRC, 2003). Where oil spills occur in natural seepage areas, such as the northern Gulf of Mexico, previously generated, remote-sensing derived maps of seepage-occurrence (Garcia-Pineda et al., 2010) can aid in discriminating natural from anthropogenic oil slicks. In general, natural seep oil emissions are highly distinct from most oil spills and involve persistent and widely dispersed oil emissions that generally result in very thin sheens (MacDonald et al., 2002).

### 1.2.2. Oil slick processes

Experienced observers can discriminate oil from biogenic slicks and estimate the amount of oil in the slick based on spatial patterns and how they change with time. These spatial patterns can be key for validation of oil slick maps derived from remote sensing data. Oil slick processes on day to week timescales—a typical oil spill response—(Fig. 1) include wind and wave advection, compression from waves and currents (into wind rows or narrow slicks), spreading and surface diffusion, sedimentation and dissolution into the water column, emulsification, evaporation, and photochemical and biological degradation (NRC, 2003). Weathering describes non-advection processes that alter the oil's chemical and physical characteristics.

Volatilization causes physical and chemical evolution of sheens and thin oil slicks on hour to day timescales (Leifer et al., 2006) with the process evolving even more slowly for thicker slicks, particularly if the upper surface develops a waxy crust (Ross & Buist, 1995). In the presence of turbulence from winds, wave breaking, or human activities, oil forms emulsions—oil/water mixtures with significantly higher viscosity and distinct physical properties (ASCE, 1996). Where fresh oil surfaces among weathered oil, the two oils tend not to mix, leading to small-scale heterogeneity (Leifer et al., 2006).

Many oil spill processes depend upon, currents, meteorology, sea state, and oil properties, like viscosity and slick thickness (ASCE, 1996; Reed et al., 1999). Currents and winds advect oil in a weighted vector sum direction (Leifer et al., 2006). For example, wind creates turbulence that increases emulsification, while dissolution is affected by water-side turbulence from wind stress, waves, and wave breaking. Wave breaking also naturally disperses oil into the water column (Farmer & Li, 1994).

Although several slick processes suggest that oil slicks should dissipate, in reality, slicks tend to accumulate at current shears due to Langmuir cells (Lehr & Simecek-Beatty, 2000) and bathymetric effects or in current convergence zones. Typical wind-driven oil patterns are asymmetric (Lehr et al., 1984) due to Fay gravitational and surface-tension driven spreading (Fay, 1971). Spreading is where an oil slick expands to maximize its surface area. In the upwind direction, spreading opposes the wind, while the two are synergistic in the downwind direction, leading to the asymmetry. Spreading is countered by inertia and viscosity. Weathering increases viscosity, decreasing spreading (Reed et al., 1999). Also affecting the asymmetry is the wind stress change as the wind passes from oil-free waters to the oil slick. Oil slicks dampen capillary and short gravity waves, lessening surface roughness (Brekke & Solberg, 2005). This alters the wind profile, decreasing wind-ocean momentum transfer, causing oil slicks to "bunch up."

### 1.2.3. Oil spill response

In an oil spill's early phases, information on the spill's location often is acquired from a few, often-conflicting observations, typically made from airborne platforms. These observations can suffer from numerous false positives, particularly given the paucity of trained observers. Thus, first observations frequently are from untrained individuals and increasingly from remote sensing, although both yield false positives (Fingas & Brown, 1997). Such incoming data can obscure the oil spill's true location and size (HAZMAT, 1996). Yet, initial response decisions and resource allocation must be made on the available information.

Initial resource allocation needs to consider likely spill size and resource deployment times and thus, the oil's future location and size when resources will arrive on-scene, i.e., spill modeling and prediction.

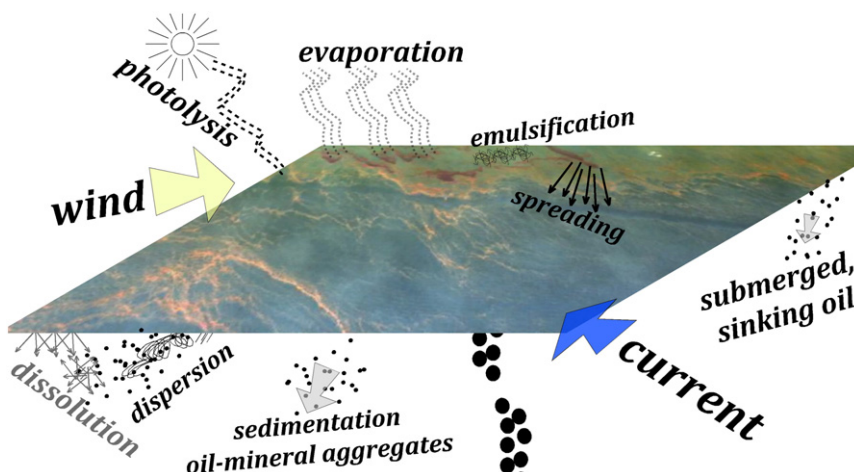


Fig. 1. Schematic of important early oil slick processes on time-scales up to a few days for a subsurface hydrocarbon spill. Oil image from AVIRIS image of the Deepwater Horizon spill.

Moreover, predicting a spill's impact, and thus the best response strategy (Reed et al., 1999), requires understanding the fate of the many oil components with different toxicities. This requires understanding the processes affecting slick chemical evolution (Riazi & Al-Enezi, 1999) and processes affecting its advection, dispersion, and transformation, as well as the sensitivity of the likely impacted coastal habitats (Jensen et al., 1990). Despite the significant impact of marine oil spills, many aspects remain poorly understood, in part due to difficulties in obtaining planned release permits, leading to a scarcity of high quality field data.

Oil spill response must address the key question: How much oil has been released? Secondary, critically important questions are: Where is the oil? What type of oil was spilled? When (and how) was the oil released? What types of ecosystems are threatened? Answers are essential for resource allocation. As oil drifts ever closer to ecologically sensitive habitats, public concern rises rapidly, particularly if the public perceives weak organizational capacity and decision making (Albaigés et al., 2006). Moreover, oil's tendency to spread and volatilize means some response techniques lose efficacy with time (Nordvik, 1995).

In a typical tanker oil spill, the ship's manifest indicates the type of oil and maximum potential oil spill volume from the hull and/or fuel tanks minus consumption during transport. Field observations on how oil is leaking from the vessel, i.e., which fuel compartments may be breached, can refine worst case release estimates downward. Although most tanker oil spills release the oil at once, oil and gas well blowout spills, like the DWH and *Ixtoc I*, are far more challenging due to continuous fresh oil release and the lack of a defined, upper-bound release estimate. Persistent releases can threaten a more extensive coastline as currents and winds shift.

Oil type is important because lighter crudes rapidly lose much of their volume due to evaporation (Fingas, 1996), reducing the volume requiring mitigation, but presenting a sinking risk (Michel & Galt, 1995), for which few mitigation technologies are available. In addition, many light, petroleum polycyclic aromatic hydrocarbons are hazardous to health (Boström et al., 2002), increasing inhalation health risks to response workers and coastal human populations.

The oil spill location in relationship to ecologically sensitive areas is important, described by an Environmental Sensitivity Index (Jensen et al., 1990), which is used for contingency planning and response decisions. Typical wind and current patterns may place greater risk for more distant than more proximal areas, with the caveat that ecological impact depends on the oil's composition when it reaches fisheries and coastal ecosystems.

#### 1.2.4. Oil slick remote sensing for oil spill response

Airborne and satellite remote sensing can aid oil spill response, yet face significant challenges. Passive approaches detect naturally occurring reflected and/or emitted electromagnetic radiation. Active approaches include light detection and ranging (lidar) and radar. Reviews by Fingas and Brown (1997, 2002) identified many promising remote sensing technologies and sensors, but generally found limited spill response applicability beyond simple visual observations that confirm known spill features. In part this is due to generally inadequate coverage, false positives, and a lack of quantitative slick mapping capabilities.

Still, satellites can play a role in oil spill response by providing preliminary spill assessment for remote locations and synoptic scale data. This role was enabled significantly by the International Charter on Space and Major Disasters Agreement, which requires that all signatory countries' space assets be provided during events such as major oil spills ([www.disasterscharter.org](http://www.disasterscharter.org), 2000). Severe limitations can arise from overpass frequency and timing and clear daytime sky requirements for passive reflective sensors (Fingas & Brown, 1997). Also of significant concern is the trade-off between coarser spatial resolution and wide swath sensors, such as MODIS (~1 km pixels), with limited swath but finer spatial resolution sensors, such as the panchromatic Quickbird (<1 m pixels). Oil slicks exhibit significant small-scale, i.e., sub-pixel, heterogeneity that can lead to slick-estimation biases for

coarse resolution sensors. Alternatively, much of the slick may be missed during infrequent narrow swath data acquisitions at finer spatial resolutions. Nested data collection can address these competing needs where the fine-scale sensor provides sub-pixel information for the synoptic view sensor; however, this requires sensor coordination.

Because oil slicks evolve on daily to hourly time-scales, swath mapping between subsequent multi-day overpasses can be ineffective. Generally, the primary satellite contribution is oil identification from radar or visual imagery prior to the arrival of on-scene investigators or outside of expected areas, (Topouzelis et al., 2007). However, frequent false positives limit utility. Consideration of ancillary data can aid spill identification and classification by experienced analysts (Ivanov & Zatyagalova, 2008). Neural network approaches can discriminate slick-like features from other dark, non-slick features, providing guidance on potential oil slicks for further investigation (Topouzelis et al., 2007). The need for confidence level classification protocols for radar-based detection has been noted; however, there is a need for contextual information, including assessment of analysis techniques, contrast, geographic location, winds and other meteorological data (Ferraro et al., 2010). These evaluations are critical to satellite utility in allocating airborne resources or indicating further satellite data analysis.

A practical reality is that acceptance of a new spill response technology requires that the technology has a proven reliability track record with well-understood physical mechanism(s), and significantly improved information relative to accepted approaches. Also critical are Rapid Response Products, where analyzed data are available in a readily usable form on the order of tens of minutes to hours after acquisition, allowing timely response decisions. Oil spills are highly dynamic and information ages rapidly, losing most utility in less than a day.

#### 1.3. Oil slick remote sensing of the DWH

The DWH release's persistence and magnitude with an estimated upper limit release of  $1.3 \times 10^9$  L oil and gas-oil equivalent (Joye et al., 2011) provided a unique opportunity for field application and integration into the response of new sensor technologies. Moreover, the slick's vast extent (order  $10^4$  km $^2$ ) precluded traditional approaches from providing a synoptic spill overview, a critical need that remote sensing partially addressed.

Airborne human observations met the primary DWH response for thick oil identification, (Section 2.1.1). These were supplemented by an expert system using multispectral imaging, which provided maps of oil thickness classes (Section 2.2.1) and hyperspectral visible to short wave infrared (SWIR) data, which were analyzed to make quantified thickness maps for the response (Section 2.2.2). The former already was operational at the beginning of the DWH spill. Limited airborne spatial and temporal coverage was extended and supplemented by satellite passive visible data (Section 2.2.3). Satellite thermal (Section 2.2.4) and airborne hyperspectral thermal data (Section 2.3.4) were collected but lacked Rapid Response Products to enable integration into the response. Airborne multispectral thermal imaging data aided thick oil identification (Section 2.3.4).

Active approaches include airborne and spaceborne SAR (Section 3.1.2) with several satellite SAR sensors offering Rapid Response Products. Post-spill analysis of spaceborne and airborne lidar data (Section 3.2.3) demonstrated remote sensing of near-surface submerged oil. Post-spill remote sensing data can support ecosystem recovery through hyperspectral vegetation maps and airborne SAR ecosystem oiling maps to monitor impacts (Section 4.1). Hyperspectral remote sensing and lidar data provided information on in situ burning and smoke (Sections 4.1.2 and 4.1.3) and demonstrated a remote sensing capability for monitoring in situ burning, although ancillary data were critical to interpretation for these applications. Thermal spectrometry provided a measure of air quality information (Section 4.2.2). Approaches such as laser-induced fluorescence (Section 3.1.3.2), which applies to thin sheens, saw little DWH application.

**Table 1**

Oil appearance and thickness.  
From Bonn Agreement (2004, 2009).

| Code | Description/appearance       | Bonn, layer thickness (μm) | ASTM, layer thickness (μm) | Bonn, liters per km <sup>2</sup> |
|------|------------------------------|----------------------------|----------------------------|----------------------------------|
| 1    | Sheen (silvery/gray)         | 0.04 to 0.30               | 0.1–0.3                    | 40 to 300                        |
| 2    | Rainbow                      | 0.30 to 5.0                | 0.3–0.5                    | 300 to 5000                      |
| 3    | Metallic                     | 5.0 to 50                  | ~3                         | 5000 to 50,000                   |
| 4    | Discontinuous true oil color | 50 to 200                  | >50                        | 50,000 to 200,000                |
| 5    | Continuous true oil color    | 200 to >200                |                            | 200,000 to >200,000              |

## 2. Passive remote sensing of oil slicks

### 2.1. Background: oil slick spectroscopy

#### 2.1.1. Visible appearance of oil slicks

In an oil spill's initial phases, its trajectory, location, and magnitude are known poorly with experienced observers and remote sensing instruments unlikely to be on site. Weather and orbital positions and remoteness may delay satellite observations and the arrival on-scene of experienced observers. Thus, initial reports often are conflicting with uncertain accuracy. This is because many common marine phenomena, including "ice, internal waves, kelp beds, natural organics, pollen, plankton blooms, cloud shadows, jellyfish, algae, and guano washing off rocks have all been reported as oil by untrained observers" (HAZMAT, 1996), as well as wind shadows, weed beds, and oceanic fronts (Fingas & Brown, 2011). Thin sheens are particularly susceptible to misidentification, as they appear similar to non-oil biological slicks. In fact, the sea surface's upper 1 mm is well described as a gelatinous biofilm (Cunliffe & Murrell, 2009).

To aid in standardizing reporting, the visual appearance of confirmed oil slicks with respect to slick thickness is defined by Oil Slick Thickness Codes (Table 1); Codes 1 to 3 are for oil slick appearances governed by optical effects, with Codes 4 and 5 based on true color (ASTM, 1996; Bonn Agreement, 2004). The thinnest slicks or sheens (Code 1) have a silvery-gray appearance due to increased reflectance relative to seawater. Rainbow slicks (Code 2) have oil thickness near to, or a few integer multiples of the wavelength of light. Metallic slicks (Code 3) have oil color but sky reflection is dominant. Differences between the Bonn and ASTM (American Society of Test Materials) codes result from not specifying how slick appearance varies with petroleum type, and viewing and solar angles (Lehr, 2010; Taft et al., 1995).

Slicks thicker than 50 μm (Codes 4 and 5) exhibit the oil's true color and thus are dominated by absorption, not sky reflectance or thin film optical processes. Because most oil is in thick slicks, ~90% according to Hollinger and Mennella (1973), the Thickness Codes provide little guidance for volume assessment of the thicker oil slick portions, which are most suitable for mitigation. Unfortunately, slick

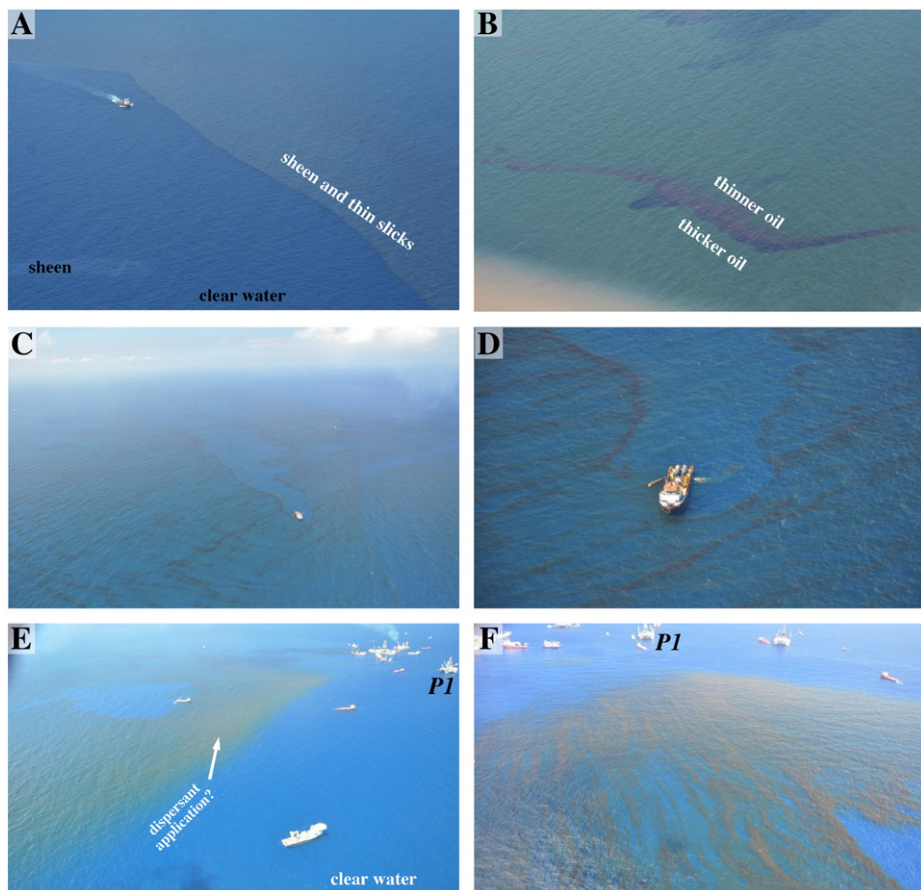


**Fig. 2.** Sample Deepwater Horizon spill aerial photos on 23 June 2010 of A Sheen and thin slick. B. Fresh surfaced oil in thin slick. C. Distant slick. D. Same as C, but closer, showing wake bunch-up and sheen coverage asymmetry. E. Dispersant application. F. Possible weak Langmuir slick organization and cloud shadows. Platform (P1) identified in E and F to aid orientation. Images courtesy of Ben Holt.

appearance in the visible spectrum varies with several factors of which thickness is not necessarily dominant (Clark et al., 2010).

For this review, we apply an operational (spill response) definition with slicks thinner than 10–50 µm termed “sheens,” while slicks thicker than 200 µm are termed “slicks.” Some oil spill mitigation strategies are ineffective against thin oil (e.g., in situ burning; skimmers). Moreover, sheens are usually too thin to emulsify, while thick, crude oil slicks readily form stable and meta-stable oil–water emulsions. Note that these definitions are approximate and depend on the oil type, spill observation approach, and response approach.

Oil slick assessment must consider sea state and sea state history, which can affect oil slick appearance. For example, oil sheens alter the sea surface appearance; however, unoiled sea surface usually appears slicked for light winds. Also, higher winds prior to observations can lead to temporary subsurface oil suspension. Even in calm seas, subsurface floating oil droplets can be obscured by surface slicks, from surface observers (Leifer, 2010, unpub observations).

#### 2.1.2. Visible spectrum oil slick assessment

Discriminating oil slicks from similar, non-oil marine phenomena strongly relies on interpretation of oil spatial patterns and appearance consistent with oil spill weathering and advection, i.e., the many

processes of oil weathering and transport (ASCE, 1996), particularly slick convergence processes like Langmuir circulation (Lehr & Simecek-Beatty, 2000) (Fig. 2F), fronts (Fig. 2A) (Klemas & Polis, 1977), bathymetric-induced current shear, and eddies. Also, response efforts such as dispersants may alter an oil slick's appearance by dispersing it subsurface (Fig. 2E), and boat wakes can thicken slicks dramatically and emulsify oil (Fig. 2D).

Sheens (Codes 1–3) contain negligible recoverable oil but can also arise from biogenic sources, and can be confused for thicker oil (Codes 4–5) at low viewing angles or under cloudy skies. At very low wind speeds (<2 m s<sup>-1</sup>), the sea surface often is covered with sheens (Fig. 3A), largely from non-petroleum sources. Natural non-oil sheens typically disperse at slightly greater winds, which are associated with capillary wave formation (Donelan & Pierson, 1987), while, oil sheens generally are more persistent and tend to “bunch up” into thicker slicks.

A key, but not definitive, spatial pattern oil indicator (Fig. 3C, D) is a point source connected to a streak-like pattern. Crude oil emulsification is a rapid process, thus outside of freshly released or surfaced crude oil (Fig. 2B), most spilled oil is found as stable or quasi-stable oil–water emulsions that significantly alter the oil's visible appearance. The slick's visible spectrum appearance depends strongly on the oil to water ratio and entrained air, and weakly on the emulsion thickness (Clark et al.,

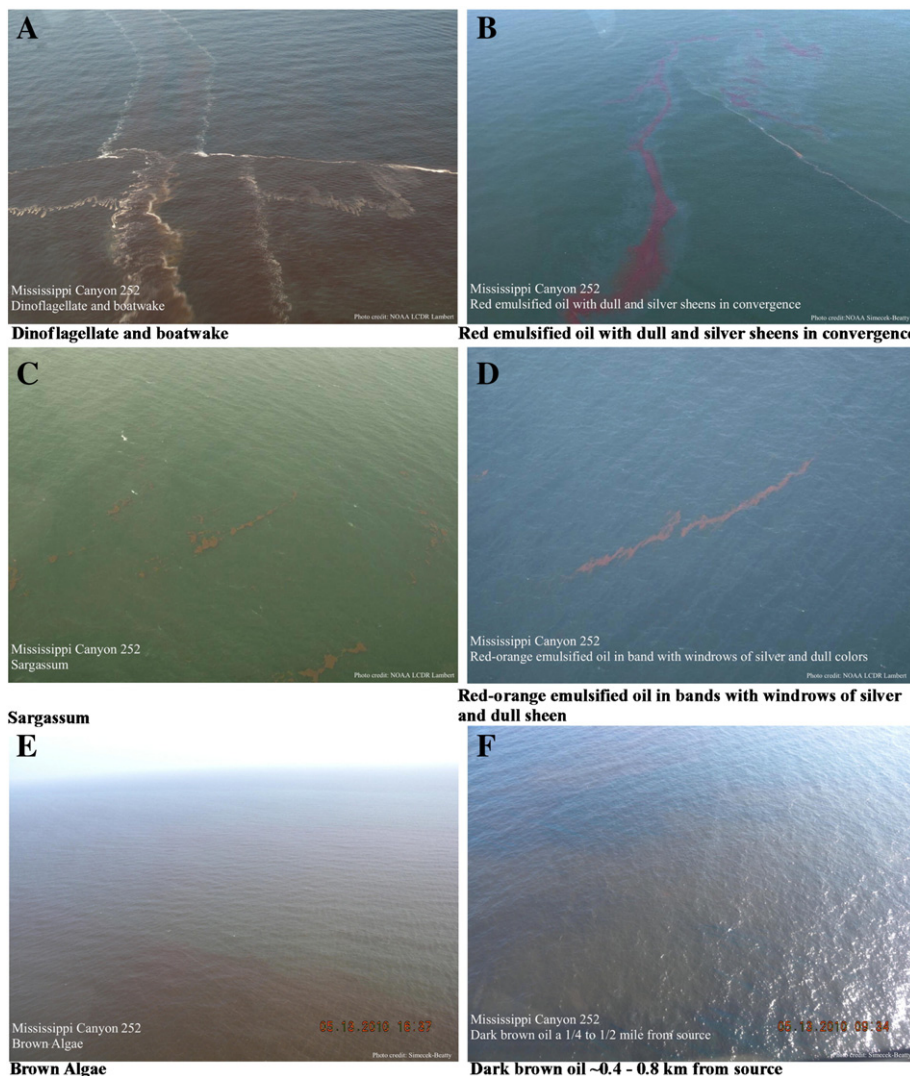


**Fig. 3.** Deepwater Horizon aerial photos of (A,C,E) false positives and (B,D,F) similar looking oil slicks. Images courtesy of Debra Simecek-Beatty.

**Table 2**  
Summary of oil spill remote sensing relevant airborne sensors.

| Instrument  | Region (bands) | Range (nm)             | Platform           | Resolution (m)                 | Cross track (pixels) | Primary link   | Full name   | Agency                              | Comment                                      |
|-------------|----------------|------------------------|--------------------|--------------------------------|----------------------|--|---|-------------------------------------|--|
| AVIRIS      | UV–NIR (224)   | 380–2500               | Twin Otter, ER-2   | 4.4–20                         | 677                  | <a href="http://aviris.jpl.nasa.gov/">http://aviris.jpl.nasa.gov/</a>  | Airborne Visible Infrared Imaging Spectrometer                    | NASA/Jet Propulsion Laboratory      | Whisk broom                                  |
| HyMap       | UV–NIR (128)   | 450–2480               | Multiple           | 3–10                           | 512                  | <a href="http://www.hvista.com">www.hvista.com</a>   | Hyperspectral MAPPING   | Hvista Corp.                        | Whisk broom                                  |
| SEBASS      | MIR, TIR (128) | 2500–5200, 7500–13,500 | Twin Otter         | 2–7                            | 128                  | <a href="http://www.aero.org/capabilities/documents/AER027_SEBASS_Final.pdf">www.aero.org/capabilities/documents/AER027_SEBASS_Final.pdf</a> | Spatially Enhanced Broadband Array Spectrograph                   | The Aerospace Corp.                 | 128 × 128 imaging element                    |
| ASPECT      | MIR, TIR (16)  | 3410–5330, 8730–11,360 | Aero Commander 1.1 | 1.1                            | 1                    | <a href="http://www.epa.gov/NaturalEmergencies/flyinglab.htm">http://www.epa.gov/NaturalEmergencies/flyinglab.htm</a>                        | Airborne Spectral Photometric Environmental Collection Technology | EPA                                 | Line scanner, flown at 1000 m                |
| ASPECT FTIR | TIR (2048)     | 1266–11,360            | 680 (twin engine)  | 9                              | 1                    | <a href="http://www.epa.gov/NaturalEmergencies/flyinglab.htm">http://www.epa.gov/NaturalEmergencies/flyinglab.htm</a>                        | Airborne Spectral Photometric Environmental Collection Technology | EPA                                 | Fourier transform spectrometer               |
| UAVSAR      | L-band         | 1,2175–1,2975 GHz      | Gulfstream 3       | 1.7–0.6 single                 | 9900                 | <a href="http://uavstar.jpl.nasa.gov/">http://uavstar.jpl.nasa.gov/</a>  | Uninhabited Aerial Vehicle Synthetic Aperture Radar               | NASA/Jet Propulsion Laboratory      | 22–65° incidence angles                      |
| HSRL        | Vis, NIR (2)   | 532, 1064              | B200 or Learjet    | –                              | 1                    | <a href="http://science.larc.nasa.gov/hsrl/">http://science.larc.nasa.gov/hsrl/</a>  | High Spectral Resolution Lidar                                    | NASA/Langley                        |  |
| CHARTS      | Vis, NIR (2)   | 532, 1064              | Twin engine        | 2/5 (topographic/hydrographic) | 500                  | <a href="http://www.jalbtcx.org">www.jalbtcx.org</a>   | Compact Hydrographic Airborne Rapid Total Survey, Optech Inc.     | US Army Corps of Engineers/JALBT CX | 3 or 20 kHz sample, to 60 m, SHOALS-3000 T20 |
| CASI-1500   | Vis–NIR (36)   | 375–1050               | Twin engine        | 0.25–10                        | 1500                 | <a href="http://www.jalbtcx.org">www.jalbtcx.org</a>   | Compact Airborne Spectrographic Imager, ITRES                     | US Army Corps of Engineers/JALBT CX | Push broom, operates with CHARTS             |

UV—Ultraviolet, Vis—Visible, NIR—Near Infrared, MIR—Mid Infrared, TIR—Thermal Infrared, JALBT CX—Joint Airborne Lidar Bathymetry Technical Center of Expertise.

2010). Often, weathered oil emulsions appear similar to algae, sargassum, and other organic materials, which may accumulate along convergence zones (Fig. 3A, C, E). Spilled oil and non-oil organic materials often can be intermixed. However, unlike non-petroleum hydrocarbons (Fig. 3C), thick oil generally is surrounded by sheen (Fig. 3B), unless the oil is heavily weathered (Fig. 3D). Furthermore, the sheen often is asymmetric with respect to wind direction (Fig. 2D), if there is wind (Fig. 3B). Brown algal blooms (Fig. 3E) and dark brown oil (Fig. 3F) can appear similar, but their patterns differ in the presence of waves. Note that the subtle wind-driven sheens in Fig. 3F are distinct from Langmuir rows in Fig. 3E, with different color variations across the brown patches in evidence.

#### 2.1.3. Visible spectrum oil slick appearance: underlying spectroscopy

Thin sheen oil optical behavior is governed by light transmission and reflection through the slick. This light includes downwelling solar radiation and upwelling reflected light and scattered light from the underlying water and oil. Oil identification is by contrast with seawater; and thus is most successful where sub-surface upwelling radiance is higher relative to specular sky radiance seawater reflection, in the range of 480–570 nm (Byfield & Boxall, 1999). These reflectances and transmittances have strong wavelength and angular dependencies with greater contrast for less oblique observations and shorter wavelengths (Otremba & Piskozub, 2004). Thickness makes a difference for thinner slicks. Wettle et al. (2009) found a steeper fall off in crude oil reflectance (greater absorption) towards blue for spectra spanning 470 to 800 nm, with increasing slick thicknesses from 10 to 133 μm. Because the goal was comparison with the 4-band, Quickbird satellite and the airborne hyperspectral HyMAP sensor, Wettle et al. (2009) did not investigate angular dependencies. Remote sensing instruments for oil spill response on airborne and satellite platforms, including acronym definitions are described in Tables 2 and 3, respectively.

#### 2.1.4. Near infrared oil slick appearance: underlying spectroscopy

Petroleum hydrocarbon spectral features in the near infrared (NIR) are dominated by a carbon–hydrogen bond, C–H, stretch and also symmetric axial and angular deformations, with a mid-infrared (MIR) fundamental near 3300 nm. The first NIR overtones are near 1720–1730 and 1750–1760 nm, with a combination band near 2370 nm, and second overtones near 1190–1210 nm for some oils (Clark, 1999; Lammoglia & Filho, 2011). These features can identify hydrocarbons. For example, Hörig et al. (2001) identified spectral differences in spectral features centered at 1730 and 2310 nm in HyMap data that distinguished between oil-contaminated and uncontaminated sand. Similar spectral features were found for a plastic tarp but not vegetation. Kühn et al. (2004) created a hydrocarbon index using radiances at 1705, 1729, and 1741 nm from the same HyMap data and found improved detection. There are features at 1390 and 1410 nm due to a first oxygen–hydrogen bond, O–H, overtone that could be diagnostic (Clark, 1999).

In reflectance, light at different wavelengths penetrates an absorbing layer to different depths due to varying absorption and scattering (Clark, 1999). This enables different wavelengths to probe an oil or oil-emulsion layer to different depths (Fig. 5), and can cause a slope or skew in an absorption feature, termed “shoulder-ness,” see schematic in Fig. 4A–D. Furthermore, the continuum—i.e., the spectrum outside the feature, is shaped by nearby water absorptions, which are affected strongly by the oil to water emulsion ratio. For oil slicks thinner than a lower thickness limit, light for wavelengths spanning the IR absorption feature penetrates the oil film and is absorbed by the underlying water. This absorption occurs approximately uniformly with wavelength with negligible scattering (Fig. 4B) leading to no layer thickness change on the reflectance spectra of the absorption feature. For oil slicks thicker than an upper thickness limit, light with wavelengths spanning the feature is absorbed and scattered by the

**Table 3**  
Summary of oil spill remote sensing relevant spaceborne sensors.

| Instrument (satellite)         | Bands (# bands) | Band range (nm) | Resolution (km)          | Swath (km)   | Revisit <sup>A</sup> (days) | Rapid response | Link   | Acronym  | Comment   |
|--------------------------------|-----------------|-----------------|--------------------------|--------------|-----------------------------|----------------|--|--|---|
| LandSat 5, LandSat 7 (8 bands) | Vis, NIR, TIR   | 450–12,500 nm   | 0.030–0.120              | 185          | 16                          | No             | <a href="http://landsat.gsfc.nasa.gov/about/">http://landsat.gsfc.nasa.gov/about/</a><br><a href="http://landsat.usgs.gov/">http://landsat.usgs.gov/</a>   | Land Satellite   | LandSat 7 had Scan Line Corrector failure   |
| LandSat TM (7 bands)           | Vis, NIR, TIR   | 450–12,500      | 0.03, 0.120              | 185          | 1–3/16                      | No             | <a href="http://landsat.gsfc.nasa.gov/about/tm.html">http://landsat.gsfc.nasa.gov/about/tm.html</a><br><a href="http://landsat.usgs.gov/">http://landsat.usgs.gov/</a>   | Land Satellite Thematic Mapper   | Rapid revisit is for nadir  |
| MODIS (Terra, Aqua) (36 bands) | Vis, MIR, TIR   | 405–14,385      | 0.25, 0.5, 1.0           | 2330         | 1–2                         | Yes            | <a href="http://modis.gsfc.nasa.gov/">http://modis.gsfc.nasa.gov/</a>  | Moderate Resolution Imaging Spectroradiometer  | 120 m in TIR band   |
| ASTER (Terra) (14 bands)       | VNIR, NIR, TIR  | 520–11,650      | 0.015/0.03/0.09          | 60           | 4–16                        | No             | <a href="http://asterweb.jpl.nasa.gov/">http://asterweb.jpl.nasa.gov/</a>  | Advanced Spaceborne Thermal Emission and Reflection Radiometer   |   |
| MISR (Terra) (4 bands)         | Vis, NIR        | 446.4–866.4     | 0.275–1.1                | 360          | 2–9                         | No             | <a href="http://www-misr.jpl.nasa.gov/">http://www-misr.jpl.nasa.gov/</a>  | Multangle Imaging SpectroRadiometer  | 9 different, simultaneous along track viewing angles                              |
| MERIS (ENVISAT) (15 bands)     | Vis–NIR         | 412.5–900       | 2.36 × 0.30–1.04 × 1.2   | 1150         | 3                           |                | <a href="http://miravi.eo.esa.int/en/">http://miravi.eo.esa.int/en/</a><br><a href="http://www.esa.int/esaEO/SEMWYN2VQUD_index_0_m.html">http://www.esa.int/esaEO/SEMWYN2VQUD_index_0_m.html</a>   | Medium Resolution Imaging Spectrometer   | Bands can be reprogrammed   |
| HICO (90 bands)                | Vis–NIR         | 390–1040        | 0.95                     | 43           | –                           | No             | <a href="http://www.nasa.gov/mission_pages/station/research/experiments/HREP-HICO.html">http://www.nasa.gov/mission_pages/station/research/experiments/HREP-HICO.html</a>  | Hyperspectral Imager for the Coastal Ocean   | International Space Station   |
| Quickbird (4 bands)            | Vis–NIR         | 450–900         | .00061/0.0024            | 16.4         | 1–3.5                       | Yes            | <a href="http://www.digitalglobe.com">http://www.digitalglobe.com</a><br><a href="http://www.satimagingcorp.com/satellite-sensors/quickbird.html">http://www.satimagingcorp.com/satellite-sensors/quickbird.html</a>   | –  | Panchromatic has higher resolution  |
| AVHRR/3 (POES) (6 bands)       | Vis, MIR, TIR   | 580–12,500      | 1.09                     | 2440         | 0.5                         | No             | <a href="http://noaasis.noaa.gov/NOAASIS/ml/avhrr.html">http://noaasis.noaa.gov/NOAASIS/ml/avhrr.html</a><br><a href="http://www.class.ngdc.noaa.gov/data_available/avhrr/index.htm">http://www.class.ngdc.noaa.gov/data_available/avhrr/index.htm</a>       | Advanced Very High Resolution Radiometer (Polar-orbiting Operational Environmental Satellites)                       |   |
| RadarSat1 (C-band)             | C-band          | 5.3 GHz         | 0.008–0.1                | 50–500       | 24                          | Yes            | <a href="http://www.asc-csa.gc.ca/eng/satellites/radarSat1/">http://www.asc-csa.gc.ca/eng/satellites/radarSat1/</a>  | Radar Satellite-1  |   |
| RadarSat2 (C-band)             | C-band          | 5.405 GHz       | 0.001–0.100              | 20–1000      | 12                          | Yes            | <a href="http://www.gsmdacorporation.com/SatelliteData/RadarSat2/Features.aspx">http://www.gsmdacorporation.com/SatelliteData/RadarSat2/Features.aspx</a><br><a href="http://envisat.esa.int/instruments/asar/">http://envisat.esa.int/instruments/asar/</a> | Radar Satellite-2  | Left and right look halves revisit time   |
| ASAR (ENVISAT)                 | C-band          | 5.331 GHz       | 0.010–1.0                | 10–1000      | 35                          | Yes            | <a href="http://envisat.esa.int/instruments/asar/">http://envisat.esa.int/instruments/asar/</a>  | Advanced Synthetic Aperture Radar (ENVironmental SATellite)  | Provides continuity with ERS-2  |
| ERS-SAR (ERS-2) (C-band)       | C-band          | 5.330 GHz       | 0.006–0.030              | 5–100        | 3/35/168                    | Yes            | <a href="http://earth.esa.int/ers/">http://earth.esa.int/ers/</a>  | European Resource-Sensing–Synthetic Aperture Radar   | Orbital adjustment with different repeat cycles Mission ended 5 Sept. 2011        |
| Cosmo SkyMed2 (ALOS)           | X-band          | 9.6 GHz         | 0.001–0.1                | 10–200       | 0.5–1.25                    | Yes            | <a href="http://www.telespazio.it/cosmo.html">http://www.telespazio.it/cosmo.html</a>  | Constellation of Small Satellites for Mediterranean basin Observation  | A constellation of 4 satellites, steerable  |
| PALSAR (ALOS)                  | L-band          | 1.270 GHz       | 0.007–0.1                | 20/40/70–350 | 46/2                        | No             | <a href="http://www.eorc.jaxa.jp/ALOS/en/about/palsar.htm">http://www.eorc.jaxa.jp/ALOS/en/about/palsar.htm</a>  | Phased Array-type L-band Synthetic Aperture Radar (Advanced Land Observing Satellite)                                | Multiple resolution modes, fast revisit by targeting. 20 km is experimental mode. |
| TerraSAR-X (X-band)            | X-band          | 9.6 GHz         | 0.001–0.018              | 5–150        | 2.5                         | Yes            | <a href="http://www.infoterra.de/terra-sar-x-satellite">http://www.infoterra.de/terra-sar-x-satellite</a>  | Terra Synthetic Aperture Radar Xband   | Has twin, TanDEM-X satellite  |
| CALIOP (CALIPSO) (2 bands)     | Vis, NIR        | 532, 1064       | 0.1                      | –            | 16                          | No             | <a href="http://www-calipso.larc.nasa.gov/">http://www-calipso.larc.nasa.gov/</a>  | Cloud Aerosol Lidar with Orthogonal Polarization (Cloud–Aerosol Lidar and Infrared Pathfinder Satellite Observation) | Vertical resolution is (0.03–0.60 km)   |
| SCIAMACHY (ENVISAT) (15 bands) | UV, Vis, NIR    | 240–2380        | 30×60–32×215, 1000, 1000 | 3            | No                          |                | <a href="http://envisat.esa.int/instruments/sciamachy/">http://envisat.esa.int/instruments/sciamachy/</a>  | Scanning Imaging Absorption Spectrometer for Atmospheric CHartographY (ENVironmental SATellite)                      | 1000 km for limb mode   |
| AMSR-E (Aqua) (12 bands)       | Microwave       | 6.925–89 GHz    | 6×4–74×43                | 1445         | 1                           | No             | <a href="http://www.ghcc.msfc.nasa.gov/AMSR/">http://www.ghcc.msfc.nasa.gov/AMSR/</a>  | Advanced Microwave Scanning Radiometer–Earth Observing Satellite   | Ceased operation 4 Oct. 2011  |

Vis—Visible spectrum, NIR—Near infrared, UV—Ultraviolet, TIR—Thermal infrared. <sup>A</sup> repeat day is maximum.

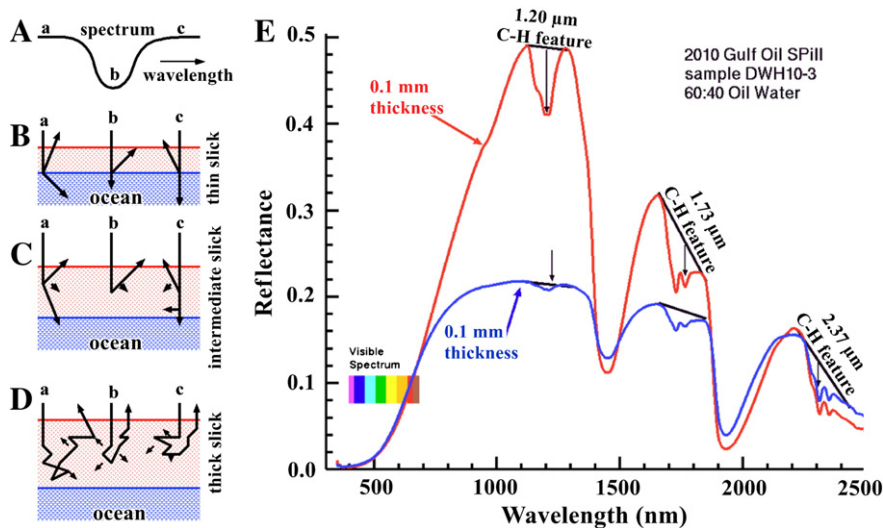


**Fig. 4.** A–D. Illustration of light scattering in oil on water. Arrow length indicates amount of scattering intensity. See text for description. E. Laboratory spectra of two different thicknesses of the same emulsions from a Deepwater Horizon oil sample. Spectra were recorded for samples in a quartz-glass window cell over a water substrate contained in a glass jar painted flat black on the inside. Black lines illustrate continuum endpoints. From Clark et al. (2010b).

oil without reaching the underlying seawater and again there is no additional layer thickness effect and no additional change in the reflectance spectra of the absorption feature. For slicks in between these two thickness limits, longer wavelength light in the absorption feature penetrates less than shorter wave-length light but the oil absorption coefficient is higher, leading to increased absorption at longer wavelengths (Fig. 4D, wavelength c) and a skew in the shape of the absorption feature.

Clark et al. (2010) showed that the overall NIR (700–2500 nm) reflectance spectrum “continuum” changes with oil thickness (Fig. 4E) and with the oil to water emulsion ratio (Fig. 5A,B). The latter arises because clear water is extremely absorbing in the NIR, and thus the spectral sensitivity to emulsification also is strongly sensitive to slick thickness. Although emulsion thickness has a small effect on visible reflectance spectra, air bubble entrainment, and the oil to water emulsion ratio affect the visible reflectance spectrum (Fig. 5).

Another factor affecting scattering in oil is the relative proportion of large branched and aromatic structure hydrocarbons, including asphaltenes, to linear aliphatic structure components that produce the noted absorption features. Laboratory studies of different oil types showed spectral variations related to oil viscosity/density including diagnostic spectral changes related to weathering and the loss of the lighter linear

fraction. This suggests a potential for remote sensing identification of oil type, at least for freshly spilled oil (Lammoglia & Filho, 2011).

#### 2.1.5. Thermal infrared oil slick appearance (emissivity)

Thermal InfraRed (TIR, 7000–14,000 nm) oil slick remote sensing has focused on discriminating oil from seawater by identification thermal contrast spatial patterns. TIR oil slick detection works by identifying a thermal contrast between the emissivity of the oil slick with the background, oil-free water emissivity and complements daytime visible spectrum reflectance by being viable at night. The thermal contrast arises due to the different emissivities of water versus oil, which depend on slick thickness (Salisbury et al., 1993). The contrast also arises from the oil's lower heat capacity, lower albedo in the visible, and different thermal conductivities.

These thermal attributes manifest as an Apparent Thermal Inertia (ATI) or temperature change resistance, defined  $ATI = (1 - a) / (T_{day} - T_{night})$ , where  $a$  is albedo, normalized by the day,  $T_{day}$ , to night,  $T_{night}$ , temperature difference. An oil slick's ATI is distinct from seawater's (Asanuma et al., 1986). During daytime, oil slicks thicker than 150  $\mu$ m appear warmer than surrounding water while thinner, detectable slicks appear cooler. This reverses at nighttime (Tseng & Chiu, 1994) with a 50–150  $\mu$ m transition (Fingas & Brown, 1997). Thinner

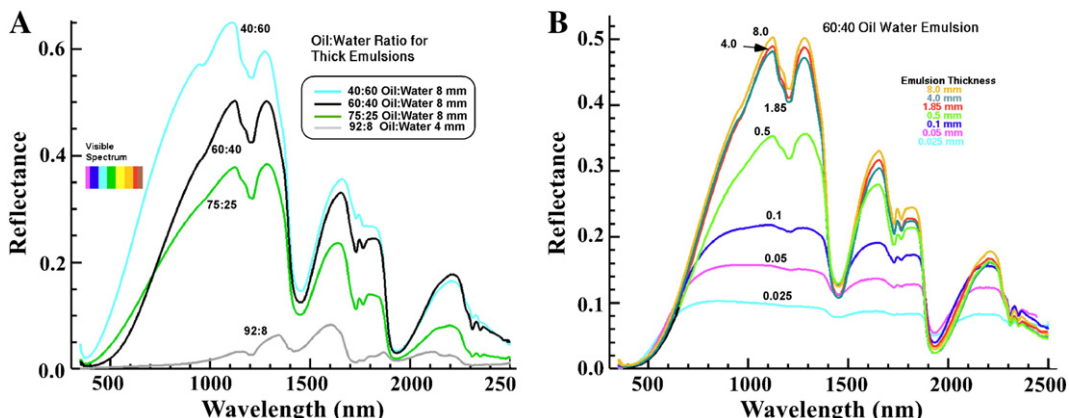


**Fig. 5.** A. Deepwater Horizon oil:water emulsion laboratory spectra for a range of oil to water ratios for thick oil. B. Spectra of a 60:40 oil-to-water ratio emulsion over a range of thicknesses. From Clark et al. (2010b).

slicks appear cooler due to the decreased emissivity of the thin oil layer relative to water (Tseng & Chiu, 1994), although the mechanism remains unclear (Fingas & Brown, 2011). Thick slicks (>500 µm) appear warmer during daytime because they are effective solar radiation absorbers, but appear cooler at nighttime as they lose heat more rapidly than the surrounding water (Tseng & Chiu, 1994).

Generally, oil sheens thinner than ~20 µm (Table 1, Codes 1–3) are not detected in TIR data (Fingas & Brown, 1997), presumably because such sheens affect sea surface temperature or emissivity (through capillary wave suppression) below sensor detection limits. Still, thin oil sheens (1–5 µm thick) were detected based on very small thermal contrasts for a sufficiently sensitive thermal imager (Noise Equivalent Delta Temperature of 0.05 °C) although significant noise could prevent slick identification (Grierson, 1998). For thin sheens, there is an apparent relationship between thickness and emissivity. As a result, under some conditions, slick TIR imagery contains far more detailed information on the slick structure and the location of thicker oil than visible imagery (Fingas & Brown, 2011).

Very thick slicks can exhibit temperatures highly different from surrounding water. In AVHRR satellite data for a 1991 Persian Gulf oil spill, daytime temperature elevations of 2–4 °C were observed. In a March 1994 Persian Gulf oil spill, daytime hotspots were 2–3 °C warmer and nighttime coolspots ~2 °C cooler than surrounding waters (Tseng & Chiu, 1994).

Oil exhibits potentially diagnostic C–H vibrational TIR emissivity features, that could reduce false positives from non-oil processes affecting sea surface temperature. These include out-of-plane double C–H deformation features at 6800 and 7400 nm and a broader C–H deformation feature at 13,300 nm (Byfield, 1998), although water vapor affects the 6800 nm feature (Salisbury et al., 1993). There also is a strong alkane feature at 9700 nm (Clark et al., 2009), which appears in heavy fuel oil (Byfield, 1998). These features vary with oil type, with lab spectra suggesting an aromatic stretch feature at 6080 nm can distinguish Brent from Gulfax crudes, while sulfur adds a signature at 14,200 nm (Byfield, 1998). Also, increasing emulsion levels led to a decrease in the strength of the 6800 and 7400 nm features (Lammoglia & Filho, 2011), suggesting potential for TIR oil slick thickness remote sensing as for NIR features (Section 2.1.4).

## 2.2. Passive oil slick remote sensing

### 2.2.1. Multispectral (visible and thermal) expert system

Expert systems can augment the limited availability of experienced observers by providing rapid image analysis for oil spill thickness estimation. An effective approach uses a neural network trained on a range of images of oil of different thicknesses, oil-free water, sunglint,

and typical sea surface features. A fuzzy logic classification algorithm produces a geo-referenced map of oil thickness classes (Svejkovsky, 2009; Svejkovsky et al., 2009). Note that significant sunglint, or surface layer reflection inherently reduces oil slick detection of any thickness.

A four VNIR channel, multispectral expert system was developed by Ocean Imaging Corp. and mapped oil thickness classes during several at-sea oil spills off the California coast and for the DWH spill. Although crude oil reflectance spectra from 300 to 1000 nm are sensitive to thickness for oil slicks thinner than 150–200 µm, they are insensitive to thickness for thicker oils (Clark et al., 2010). To address slicks thicker than 2 mm, the system incorporates a TIR camera. Both lab and at-sea tests showed that oil sheens, which are detectable in the visible wavelength range, generally are not discernable in TIR images; however, thicker films appeared either cooler or warmer (at progressively thicker accumulations) than the surrounding water (Svejkovsky, 2009; Svejkovsky et al., 2009), in agreement with Salisbury et al. (1993). Operational daytime use during several California oil spills (Fig. 6) consistently showed that the thickest oil features were cooler than the surrounding water surface, suggesting maximum oil film thicknesses less than the ~50–100 µm transition from cooler to warmer emissivity for typical mid-latitude daytime, clear-sky, low to-moderate wind conditions (Svejkovsky, 2009).

### 2.2.2. Quantitative oil slick imaging spectroscopy

Thick Gulf of Mexico's oil emulsions were mapped in Hurricane Katrina impacted areas using AVIRIS NIR oil spectral signatures (Swayze et al., 2007), demonstrating a potential to map quantitatively oil-to-water ratios in thick emulsions. DWH AVIRIS data were corrected for the solar spectrum, atmospheric gas absorptions, and aerosol scattering features using ACORN (Atmospheric COrrection Now, <http://www.imspec.com>) radiative transfer calculations and vegetation-free calibration spectra of a dry beach/airport tarmac, measured by a portable ASD spectrometer. The Tetracorder spectral identification and specialized DaVinci command-line software (Clark et al., 2003) then mapped oil slick volume (Clark et al., 2010) in each AVIRIS pixel by identifying the best fit to an oil-to-water emulsion and oil thickness spectral library. This resulted in maps of oil slick thickness, oil-to-water ratio, sub-pixel spatial coverage, and ultimately slick oil volume. Using oil hydrocarbon spectral absorption features allowed positive oil detection, greatly reducing false positives.

### 2.2.3. Satellite visible oil slick remote sensing

Multispectral instruments like MODIS aboard the sun-synchronous Terra and Aqua satellites aided DWH spill response due to its synoptic view (2330 km), rapid revisit time (twice daily), and near real-time Rapid Response Products. The European Space Agency's MERIS

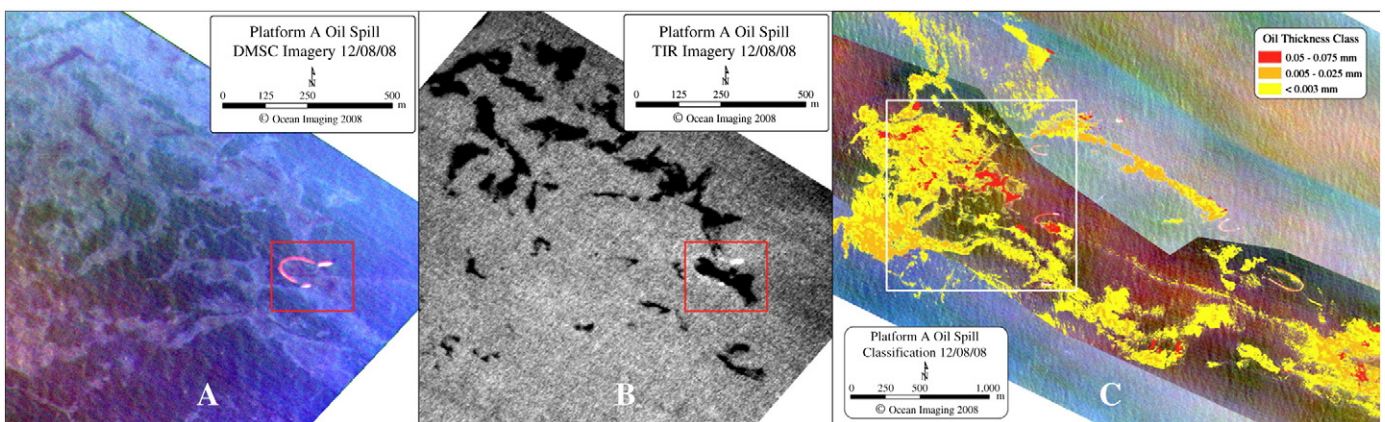


Fig. 6. A. Multispectral visible and B. Thermal IR (TIR) images, and C, multiple flight line oil thickness classification distribution estimation for oil slick in the Santa Barbara Channel, California with Ocean Imaging Corp.'s aerial oil mapping system. Red square shows boom-towing vessels and a thick oil patch. White square shows location of images A and B.

instrument also provides true color Rapid Response Products, but less frequently (3 day). MODIS and MERIS visible spectrum oil identification primarily is based on sunglint (Fig. 10); thus, solar geometry and the wave field are important. Specifically, slick detection is from modification of the wave field slopes and thus, sunglint (Adamo et al., 2009) and because slicked surfaces have higher reflectance than pure water. The latter suggest other processes could be important (Swayze et al., 2007). For example, Adamo et al. (2009) found better slick discrimination for longer wavelengths with greater sunglint sensitivity for MERIS than MODIS for the Mediterranean Sea. The MISR sensor provides views with 0.275–1.1 km pixel resolution at nine different along-track viewing angles. Using off-nadir viewing in the red band improved oil slick detection compared to MODIS in Lake Maracaibo, Venezuela, where the viewing angle (26° forward) matched most closely the specular reflection angle (Chust & Saggarminaga, 2007). This arises because oil slick contrast varies with viewing geometry (Otremba & Piskozub, 2004).

The Landsat 5 TM and Landsat 7 ETM+ have 0.015–0.12 km pixel resolutions, providing significantly higher spatial resolutions, but a narrower swath width (185 km) and a relatively infrequent revisit schedule (16-days). Also, a failed scan-line corrector has impacted ETM+ data since 2003. Landsat data have been used to map oil slicks, although the coarser temporal sampling makes it unsuitable for slick

monitoring (Bentz & Pellen de Miranda, 2001). Still, Landsat data could aid extrapolating airborne slick data to larger scales in certain situations.

#### 2.2.4. Satellite thermal infrared oil slick remote sensing

TIR oil slick analysis has significant challenges absent ancillary information, because sea surface temperature anomalies arise for many reasons, including upwelling flows, convergence zones, river outflow, different water masses, and wind history. Oil seepage slick identification was attempted from ATI analysis of two day (ASTER) and two night (MODIS) TIR scenes offshore coastal China. The analysis results were unclear because other factors affect sea surface temperature (Cai et al., 2011), showing the need for larger data sets. Also, ATI requires day/night slick comparison, although slick advection can change patterns on sub-daily timescales.

#### 2.3. Oil slick passive remote sensing of DWH

##### 2.3.1. Airborne oil slick remote sensing data collection

A NASA-led, multiagency-university effort including USGS, NOAA, Univ. of Calif., Santa Barbara, Desert Res. Inst., Univ. of Calif., Santa Cruz, and Univ. of Calif., Davis, was mobilized to acquire AVIRIS data for DWH using a NASA Lockheed ER-2 starting 6 May, and then on a

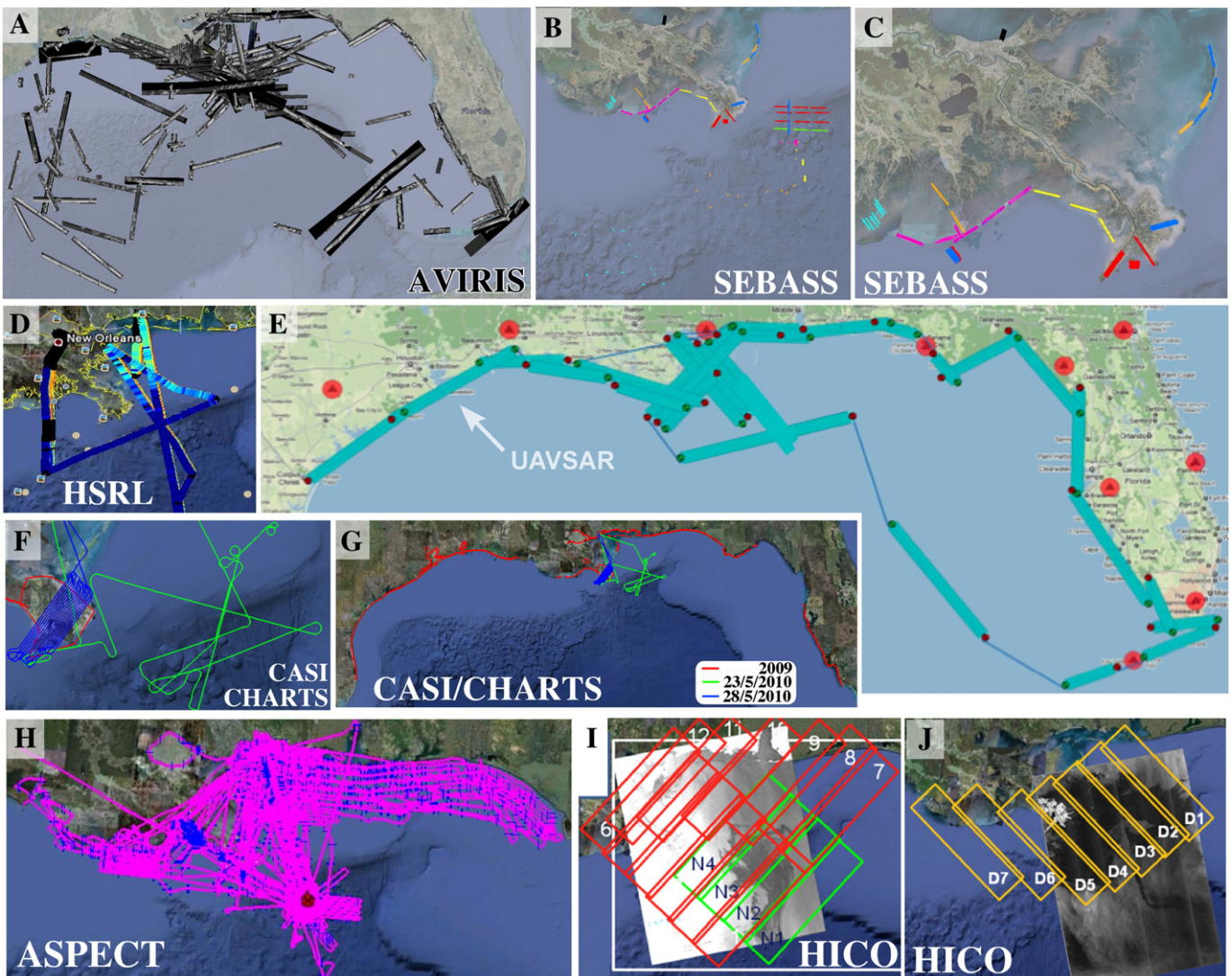


Fig. 7. DWH airborne remote sensing coverage in 2010 by A, AVIRIS, B and C, SEBASS, D, HSRL lidar, E, UAVSAR, F and G, CHARTS lidar concurrent with CASI (inset shows Gulf-wide data) for 2009 and 2010, see legend, H, ASPECT. I and J, Spaceborne HICO coverage. See Tables 2 and 3 for Acronyms.

lower altitude DeHavilland Twin Otter in July. AVIRIS collects radiance from 380 to 2500 nm in 224 channels with ~10-nm bandwidth (Green et al., 1998). AVIRIS data collection focused on: 1) oil slick imaging spectroscopy in support of the oil spill response, 2) to confirm potential oil slicks from satellite or model predictions using the ER-2 capabilities, and 3) coastal imagery analysis to understand the spill's ecosystem impacts. The latter involved successful collection of coastline data prior to the arrival of oil and repeat acquisitions after oil inundation. A total of 4 billion pixels covering over 400,000 km<sup>2</sup> were collected over 41 flight days (Fig. 7A). Same day, quick-look Google Earth RGB images were provided to NOAA and the incident command to aid response decisions and next-day flight plans (Bradley et al., 2011).

Hyperspectral TIR data (7600–13,500 nm) were collected by the SEBASS sensor onboard a Twin Otter in 128 bands (Hackwell et al., 1996). 145 flight lines were flown over 8 flight days (20–27 May 2010) covering ~700 km<sup>2</sup> with pixel sizes ranging from 1 to 5 m (Fig. 7B, C). Whenever feasible, SEBASS and AVIRIS flight lines were coordinated. TIR and MIR multispectral data were collected by the ASPECT sensor suite (Shen & Lewis, 2011), which records in 8 TIR and 8 MIR bands at 1.1-m resolution, during 75 separate flight days (Fig. 7H).

Hyperspectral 36-band data was collected by a CASI-1500, imaging spectrometer, as part of the integrated airborne Compact Hydrographic Airborne Rapid Total Survey (CHARTS) sensor suite, at 1-m spatial resolution in the 380 to 1050 nm range, contemporaneous with the CHARTS lidar. Prior to and following the DWH oil spill, ~2800 km<sup>2</sup> of concurrent hyperspectral, lidar, and aerial imagery were collected over impacted areas in southeast LA and along the northern Gulf of Mexico as well as coastal mapping in 2009 (Fig. 7F, G).

Spaceborne hyperspectral data were collected by HICO from the International Space Station. HICO measures in 102 bands from 380 to 1080 nm at 90-m resolution (Lucke et al., 2011), although data

quality is low for wavelengths longer than 800 nm (Sonia Gallegos, Naval Res. Lab., Pers. Comm., 2011). HICO imaged 200,000 km<sup>2</sup> during the DWH, including acquisitions (Fig. 7I, J) at far higher spatial and spectral resolutions than other spaceborne multispectral imagery. HICO and CASI DWH data analyses are in progress.

### 2.3.2. Multispectral oil slick thickness classification of DWH

The Ocean Imaging Corp.'s expert system collected data almost daily for the DWH spill, generally in areas surrounding the DWH well. One important consideration for aerial mapping is spatial coverage, which can be limited by low platform altitude and a narrow field of view. Producing a continuous map of the entire oil spill often necessitates mosaicing of images from multiple overlapping flight lines (Fig. 8A), during which time the spill may have evolved.

Sunglint reduces the expert system's ability to discriminate thick from thin oil, thus data generally were acquired for sufficiently low solar elevation (early and late daytime), significantly limiting acquisition time. Although, this may not be limiting during a small or moderate spills, they were very limiting over a very large release like the DWH spill. Therefore, specific spill areas were targeted in support of specific recovery operations, such as the DWH spill source area (Fig. 8). Note the good agreement between MODIS images from two days prior and post the 29 May 2010 data acquisition and how small a fraction of the spill could be surveyed.

The thermal channel greatly aided thick oil classification due to the high thermal contrasts observed. Large oil features often were observed with apparent temperatures up to 5 °C warmer than the surrounding ocean surface, indicating much thicker oil slicks. Surface observations reported oil more than ~2 cm thick (Gregg Swayze, 2010, unpublished observations). Thermal contrasts were larger than observations of the Gulf War oil spill (Tseng & Chiu, 1994), most likely from the vastly finer airborne spatial resolution compared to the AVHRR.

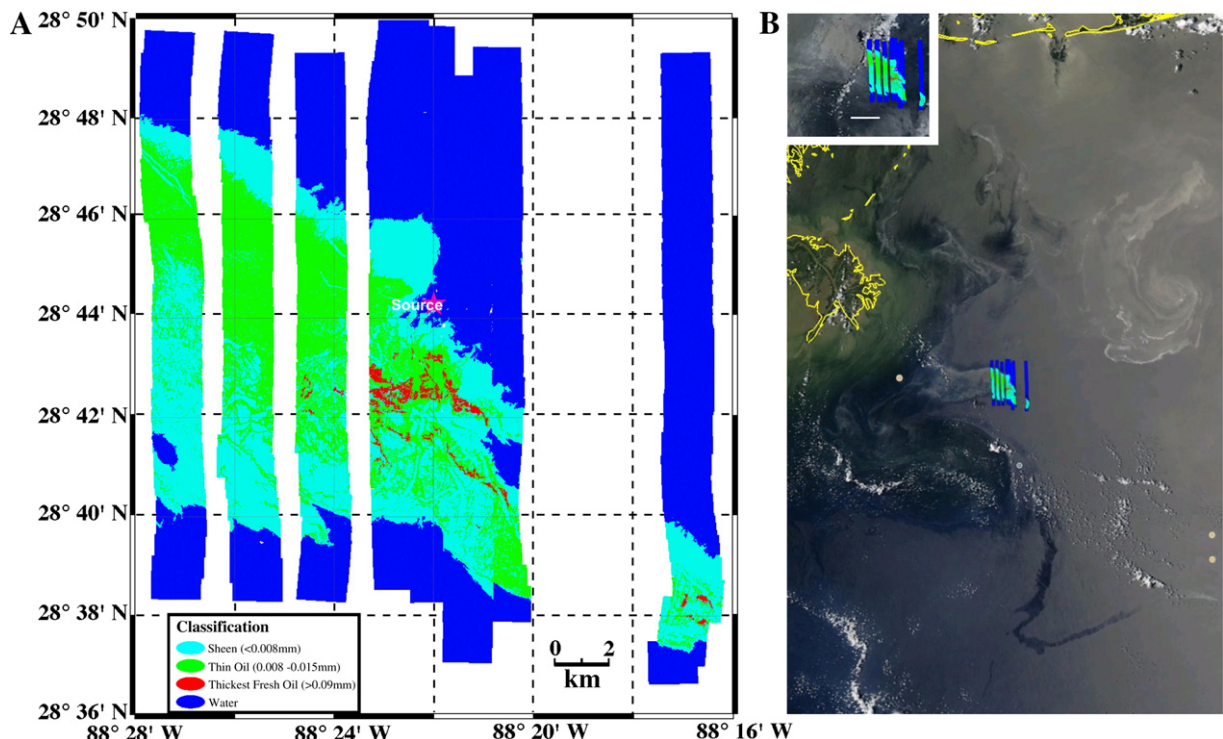


**Fig. 8.** A. Oil distribution and thickness map from expert system over the Deepwater Horizon spill source region on 29 May 2010. Imaging flight lines were offset purposefully to increase the mapping coverage area during the time available in a single flight mission. Length scale and data key on panel. B. MODIS satellite imagery for 27 May 2010 with superimposed oil thickness map. Inset MODIS satellite image for 30 May 2010 with superimposed oil thickness map. Yellow bar is 10 km. Oil thickness maps courtesy of Ocean Imaging Corp. (For interpretation of the references to color in this figure legend, the reader is referred to the web version of this article.)

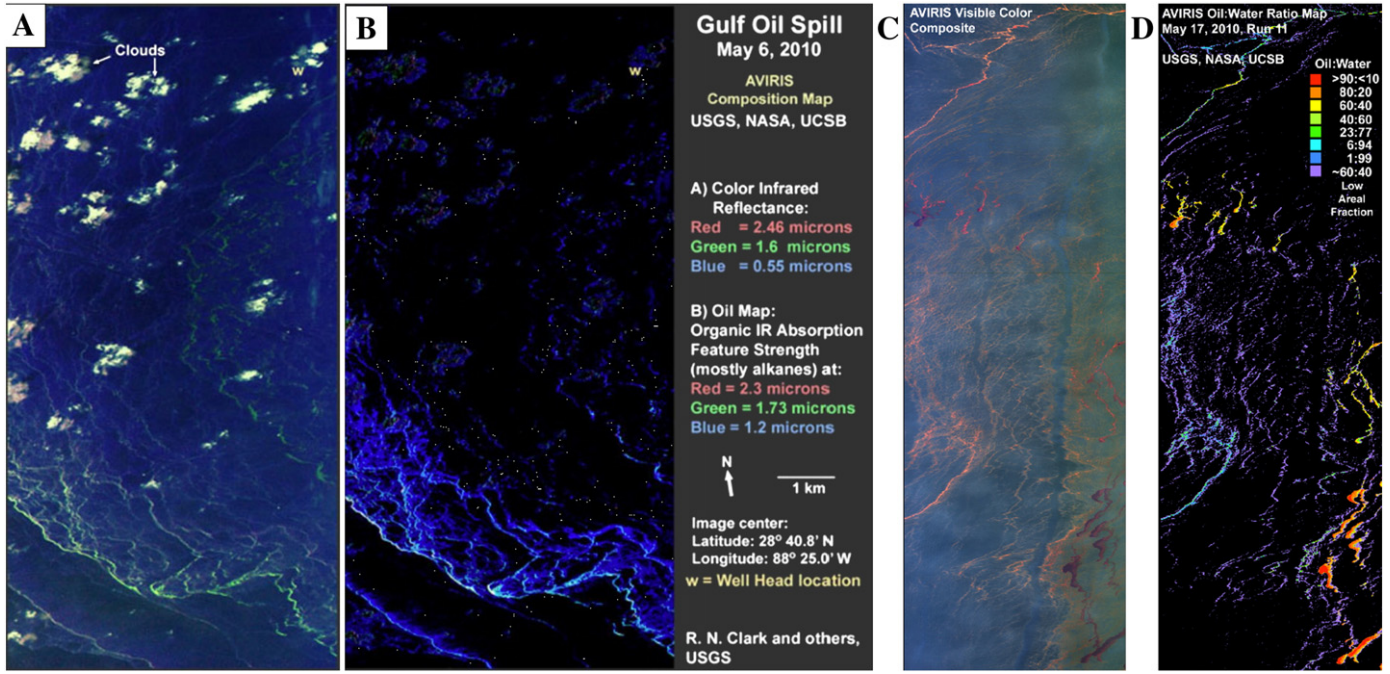


**Fig. 9.** A. False color AVIRIS image, including clouds in scene. B. RGB map of band absorption strength, which correlates with oil thickness. C. True color AVIRIS oil scene. D. Tetra-color AVIRIS oil-to-water emulsion ratio map.

From (Clark et al. 2010).

### 2.3.3. Hyperspectral quantitative oil slick mapping of the DWH

Oil thickness and oil to water emulsion ratios were derived from oil absorption features in the NIR with each absorption feature probing different oil slick thicknesses. A RGB mapping of the absorption features depths allowed qualitative visualization of spatial patterns related to thickness (Fig. 9B). The resultant map captured the spatial asymmetry (bunching up) from wind stress and oil spreading (Fig. 9B). The derived oil-to-water emulsion map (Fig. 9D) indicated that most thick oil slicks were heavily emulsified (weathered) except for large patches a few kilometers downcurrent from the incident site. A consistent data interpretation is that fresh oil was surfacing several kilometers distant from the incident site at this time in a

relatively compact footprint (100s of meters) Downcurrent direction was from current data at the DWH site (NOAA, 2010a). This explanation is also consistent with ASPECT observations of a persistent methanol plume within a few kilometers of the DWH well (discussed in Section 4.1.4) and airborne atmospheric samples that showed a similar size-scale plume of volatiles from the vicinity of the spill site (Ryerson et al., 2011; Tom Ryerson, NOAA, Pers. Comm., 2011).

### 2.3.4. Airborne thermal infrared oil slick mapping of the DWH

For broadband TIR systems, high spatial resolution is important as sub-pixel emissivity variability is assumed to be negligible, although oil slick heterogeneity suggests this assumption may be inaccurate

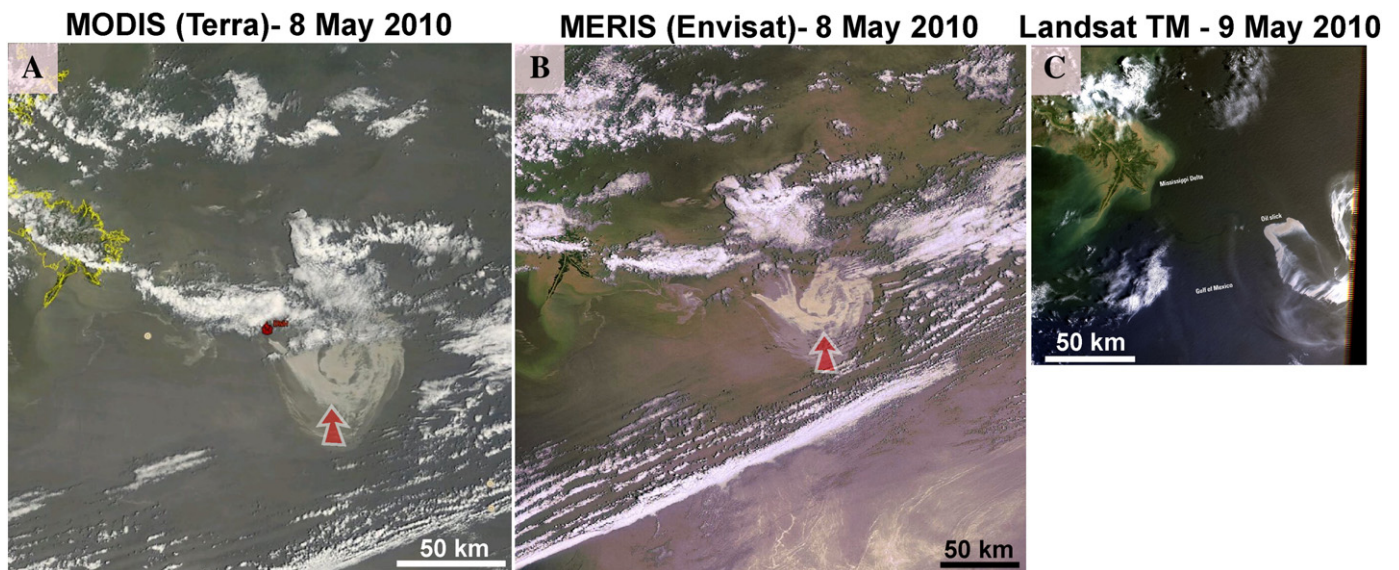


**Fig. 10.** Small image subset of MODIS and MERIS, and a Landsat 5 TM image of the Deepwater Horizon (DWH) spill on 8 and 9 May 2010. Red fire icon shows DWH site. Red arrow discussed in text. (For interpretation of the references to color in this figure legend, the reader is referred to the web version of this article.)

(Fingas & Brown, 2011). Airborne hyperspectral TIR imagers address these deficiencies, although such systems are uncommon. The multi-spectral ASPECT sensor suite discriminated between oil and seawater based on emissivity and was insensitive to features such as algae. The band centered at 11,245 nm provided the highest contrast images for discriminating oil from water, but highlighted non-oil thermal sea surface patterns. (Shen & Lewis, 2011) that can appear similar to oil in the visible range of the spectrum (e.g., Fig. 3).

### 2.3.5. Satellite oil slick remote sensing of the DWH

True-color MODIS imagery (Fig. 10) was important in the DWH response due to the spill's vast extent and the accessibility of Rapid Response Products. In conjunction with the less frequent revisit data from MERIS, high quality visible satellite imagery was available every few days, although clouds were a frequent problem. Although separated by a few hours, the MERIS and MODIS spill patterns changed significantly, with contiguous areas in MODIS appearing wispy in MERIS (Fig. 10, red arrow) presumably because of different illumination geometry and the greater sunglint sensitivity of MERIS. Although the Landsat TM (Fig. 10C) and ETM+ have far higher spatial resolutions, their narrower swath and less frequent revisit (16 days) prevented significant use during the DWH spill, particularly given the northern Gulf's cloudiness.

AVIRIS data confirmed that areas where MODIS showed wispy structures (Area B) primarily were thin sheens with a few thick oil slicks covering a tiny fraction of the sea surface. In contrast, apparently homogenous and contiguous oil areas (Area A) contained significant thick oil that still occupied only a small fraction of the sea surface (Clark et al., 2010). Overall, AVIRIS revealed that most MODIS slick pixels were mostly covered by thin sheens. On 17 May DWH oil was transported south towards the loop current (Fig. 11A, red arrow), while an associated flow transported more southerly waters northward (Fig. 11A, dashed arrow). The latter did not transport oil (Area D), yet shows characteristics similar to Area B. AVIRIS data showed that the slick's southerly tail (Area C) contained few thick oil slick patches, tens of meters wide; with most of the feature being sheen. Stronger sunglint here leads to a visual appearance that could be interpreted incorrectly as from more oil than Area B. Finally, where the tail turned northwards (Area E), scene illumination geometry and/or surface wave dampening cause the slick to appear darker. Combining MISR's nadir and 26° forward views in the red band showed subtle slick structural details (Fig. 11C). MISR lacked a Rapid Response Product and was

concurrent with MODIS (same cloud cover) and so did not contribute to the DWH response.

During DWH, satellite TIR was not used significantly, probably due in part to a lack of TIR Rapid Response Products and the need for better TIR data interpretation at satellite resolution.

## 3. Active oil slick remote sensing

### 3.1. Background: active oil slick remote sensing

#### 3.1.1. Synthetic aperture radar oil slick observations

SAR data from airborne and satellite (SSAR) platforms are used widely for surface wave detection, and because oil dampens waves, oil slick detection (Brekke & Solberg, 2005; Fingas & Brown, 2011; Holt, 2004). Radar oil slick studies date to 1969 and identify changes in surface wave properties due to oil dampening. Specifically, oil and other surfactants reduce both the surface tension and the effect of wind friction on the ocean surface, which results in a reduction and shift of short gravity and capillary waves to shorter wavelengths along with an effective reduction of wave growth. This causes a reduction in the radar backscatter from the ocean, which primarily arises from Bragg scattering by surface waves with similar wavelengths to the microwave radiation. Sheens thinner than 1.0 μm were detected for calm seas (winds to ~1.5 m s<sup>-1</sup>) for a controlled spill in the Santa Barbara Channel in 1970 with greater sensitivity for vertical polarization (Pilon & Purves, 1973). These thin oil sheens appear to affect primarily waves from 0.12 to 0.7 Hz, spanning capillary waves to short gravity waves. However, extensive slicks can dampen longer ocean waves (Hühnerfuss et al., 1983). Alcohols and other surfactant films induce maximum dampening in the range of 2–10 Hz (Trivero & Biamino, 2010).

Over the years, many studies have investigated oil releases and other substances emulating oil releases with SAR and scatterometers, including multiple frequency and multiple polarizations from aircraft and towers (Gade et al., 1998a; Hühnerfuss et al., 1983, 1996; Wismann et al., 1998). Most showed increased oil-damping attenuation associated with higher radar frequency; some also identified oil-induced scattering unrelated to Bragg scattering. Singh et al. (1986) found a strong incidence angle dependency of the backscatter strength for a planned oil release with a peak at 30–50° depending on frequency and sea state.

Previous studies have shown that C-band SAR is most sensitive to thin slicks in the wind speed range of 3.5 to 7 m s<sup>-1</sup> (Garcia-Pineda

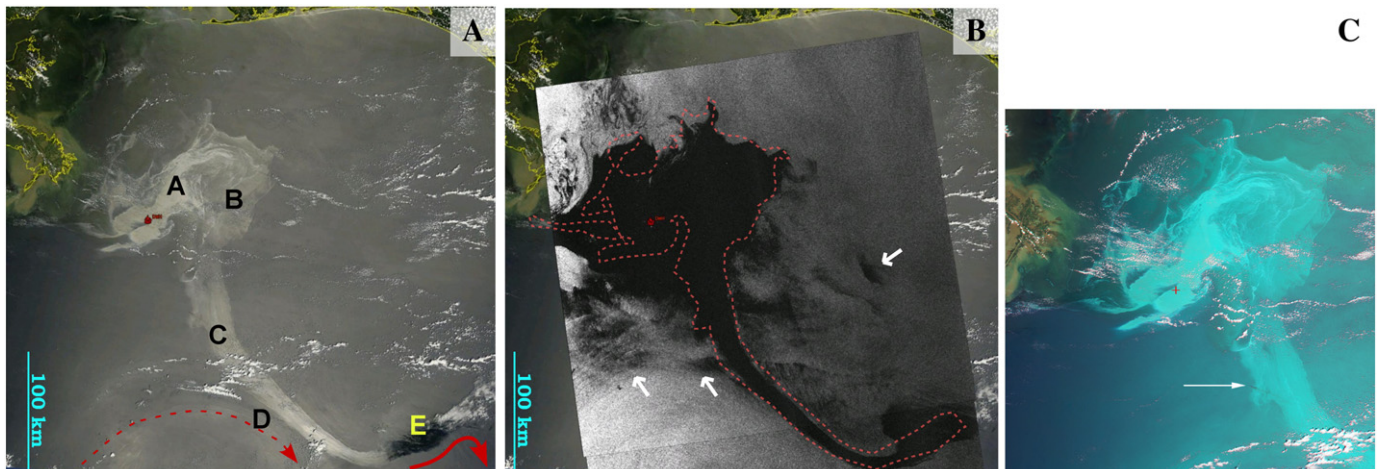


**Fig. 11.** A. MODIS Terra image and B, RADARSAT-2 SAR image of the Deepwater Horizon spill, acquired 17 May 2010 at different times. Note greater spatial extent of the SAR-identifiable spill in B (dashed red line shows oil slick outline from A, white arrows indicated false positives). C MISR false color image based on combination of nadir viewing blue and green with 26° forward red band, arrow indicates smoke from in situ burn (MISR 2010). See text for discussion. (For interpretation of the references to color in this figure legend, the reader is referred to the web version of this article.)

et al., 2009) with the detection threshold wind speed increasing to 8–12 m s<sup>−1</sup> with increasing slick thickness (Espedal, 1999; Gade et al., 1998a). An exception is for wind speeds of 5–6 m s<sup>−1</sup> where sheens disperse but thicker slicks remain as patchy areas (Jones, 2001). The threshold wind speeds for significant Bragg backscatter for different radar bands depend strongly on radar frequency, incidence angle, and ocean surface temperature, but weakly on ocean salinity (Donelan & Pierson, 1987). At very low wind speeds (<2 m s<sup>−1</sup>) the sea surface microlayer is well developed and flat because winds are too weak to roughen the sea surface through capillary wave formation (Thorpe, 1995). Thus, calm seas exhibit reduced radar backscatter and appear similar to backscatter for an oil-slicked surface, lacking contrast for slick detection (Trivero & Biamino, 2010). Similarly, white capping disperses oil and thus surface roughness depends on wave-breaking bubbles, rather than capillary waves, preventing SAR from distinguishing oil slicks at high wind speeds (Gade et al., 1998b). Wind shadowing and internal waves and rain can cause interference (Espedal, 1999; Jones, 2001), although the latter sensitivity is decreased for C-band compared to X-band (Brown et al., 2003a).

SAR data do not allow clear discrimination between oil slicks (natural or anthropogenic) and biogenic slicks (DiGiacomo et al., 2004; Gade et al., 1998b), another source of false positives. This reduces SAR utility for oil spill identification because SAR data commonly show slicks in coastal waters due to vegetation such as kelp, fluvial run-off, coastal boating, and natural oil seepage (DiGiacomo et al., 2004). Biogenic and petroleum slicks both accumulate in current and eddy shears, creating false positives (Shi et al., 2008). The ability of multi-frequency SAR to differentiate between planned biogenic and a petroleum slick was tested for a planned spill and was successful for low wind speeds, where biogenic slicks were monomolecular (Gade et al., 1998b). It is unclear if the differences between biogenic and thin oil sheens relate to sub-pixel slick spatial distribution or to chemical properties. Interestingly, heavier crude oil exhibited stronger damping curves (backscatter depression versus Bragg wave number, which can be derived from multi-frequency systems) than light oils whose damping curve is similar to biogenic slicks. This suggests that future multifrequency systems could discriminate thin sheens from thick, heavy oil slicks (Wismann et al., 1998), although further research clearly is needed.

SSAR has been used to study natural oil seepage in the northern Gulf of Mexico from persistent slicks (Garcia-Pineda et al., 2009) and their general spatial patterns (Hu, Li, Pichel, & Muller-Karger, 2009). Such techniques can also identify platform and pipeline leakage. Challenges arise in heavily trafficked production regions, such as the northern Gulf of Mexico. Ships also create turbulence wakes that resist capillary wave formation, appearing dark in SAR data and emit diesel during normal operations (Lu et al., 1999). Just 10 L (0.01 m<sup>3</sup>) of oil can create a contiguous SSAR-detectable (i.e., 0.1 μm thick) slick 50-m wide by 2-km. Estimated mean oil tanker release of bilge oil is 20 L day<sup>−1</sup> (NRC, 2003).

Despite many false positives and that current SSAR cannot discriminate sheens from thick oil (Fig. 11B), high spatial resolution (<150 m) SSAR contributes to oil slick early warning and provides data during periods of cloudiness. Key to effective early warning is reducing false positives through repeat imagery, feature extraction, and ancillary information like platform location, weather, wind speed and direction, etc. Solberg et al. (1999) identified correctly 94% of oil SAR slicks (validated by aerial overflights), but prior knowledge was key. False positives tended to occur as thin piecewise linear slick images, or in areas with very heterogeneous or low contrast background SSAR return (Brekke & Solberg, 2005). In studies of natural seeps (Garcia-Pineda et al., 2009) and identification of platform spills (Espedal, 1999), ancillary data plays a critical role in improving SSAR data interpretation. Repeat SSAR acquisitions also have been used for numerical oil spill model validation showing the need for improved model parameterizations of basic oil spill processes (Cheng et al., 2010).

### 3.1.2. Airborne and spaceborne synthetic aperture radar

Airborne SAR can map areas of interest at high spatial resolution (<10 m), with faster repeat times than SSAR, playing a key spill response role when cloud cover, foul weather, or nighttime acquisition requirements restrict other approaches. These advantages have been used in planned oil release studies (Gade et al., 1998a). The UAVSAR airborne L-band SAR uses quad polarization to image a 22-km swath width at 1-m (along-track) × 1.7-m (cross-track) single look resolution (Hensley et al., 2009). L-band wavelengths are longer (1–2 GHz, 15–30 cm free space wavelength) and have lower signal alteration from propagation through the atmosphere than airborne X- or C-band frequency instruments, even under cloud-free conditions. UAVSAR is a low noise instrument with a noise equivalent sigma zero of −53 dB at the point of maximal antenna gain, degrading to −40 dB in the near and −35 dB in the far range (Jones et al., 2011). Calibration is 1 dB absolute and 0.5 dB relative (channel to channel).

SSAR provides continuous available, synoptic-scale imagery (Fig. 11B) for early warning with newer, steerable sensor satellite systems that improve revisit times (Brown et al., 2003a). Coverage has improved significantly in the last decade with increases in the number of SSAR systems in orbit, such as the COSMO-SkyMed's 4-satellite constellation, which produces a privately available Rapid Response Product. Recent polarimetric radar satellite instruments have higher spatial resolution, aiding false positive discrimination, e.g., Envisat's ASAR with 30-m resolution which has a publicly available Rapid Response Products, RADARSAT-2, with 3 to 100-m resolutions, and ALOS PALSAR with 7-m azimuthal resolution in high-resolution mode. In some cases, polarimetric SAR exhibits significantly different co-polarized signatures for slick-free and slick-covered sea surfaces, reducing some false positives (Migliaccio et al., 2009).

### 3.1.3. Laser oil slick remote sensing

**3.1.3.1. Lidar oil slick remote sensing.** Lidar is based on the differential time-of-flight of light pulses and often is used for topographic and bathymetric mapping. However, lidar also can detect backscatter from water-column scatterers. For example, lidar and sonar-derived maps of fish schools show good spatial agreement, except where lidar observe phytoplankton layers (Carrera et al., 2006).

The CHARTS integrated airborne sensor suite system includes a topographic/bathymetric lidar, a CASI-1500 hyperspectral sensor, and a RGB digital camera (Duncan Tech-4000) with 0.2 to 0.5-m resolution. The CHARTS system surveys coastal areas as part of the National Coastal Mapping Program (Fig. 7G). A CHARTS survey consists of topographic data from the shoreline to 0.5-km onshore at 1-m spot spacing with ±0.15-m elevation accuracy and bathymetric data from the shoreline to 1-km offshore (or laser extinction) at a 5-m spot spacing with ±0.3-m elevation accuracy. Gridded data map anthropogenic and natural coastal changes through repetitive surveys. Because bathymetric laser pulse returns are measured throughout their transit through the water column, reflective and absorptive layers can be identified, allowing for the detection of surface and submerged oil.

Lidar can remotely sense oil-related changes in surface characteristics. For example, ocean surface roughness and slick affected backscatter are measured by the near nadir-pointing CALIOP lidar aboard the CALIPSO satellite. Although CALIOP primarily is an atmospheric profiler, it can be used to study backscatter from the ocean surface in its two bands at 532 and 1064 nm. Specifically, the sea surface roughness can be accurately calculated from satellite-derived winds from AMSR-E, a passive microwave radiometer, to predict lidar backscatter (Hu, Winkler, Vaughan, et al., 2009). Where the model-calculated lidar backscatter diverges significantly from observed backscatter, the sea surface is described poorly by the model, leading to an inference of oil.

**3.1.3.2. Laser fluorescence oil slick remote sensing.** Laser-induced fluorescence (LIF) has been used to detect surface oil slicks. Here, an airborne ultraviolet (UV) laser that typically operates in the range of 300–355 nm (Brown, 2011) illuminates the ocean, exciting petroleum compounds in an oil slick. A multi-channel receiver records the fluorescence spectrum, generally from 300 to 650 nm with broad peaks centered around 420–480 nm. Different oil types have distinct fluorescence spectra (Brown, 2011) with light oils fluorescing in the blue and heavy oils fluorescing towards the green (Hengstermann & Reuter, 1990). Where the oil slick is thinner than 10–20  $\mu\text{m}$ , water-column organic material fluorescence produces a broad peak at 420 nm that can interfere with oil signatures (Fingas & Brown, 2011). Chlorophyll fluorescence sharply peaks at 685 nm and is easily discriminated from oil (Hengstermann & Reuter, 1990). Synchronized range gating can prevent laser backscatter into the detector, minimizing ambient radiation input. Where the time signal is recorded, submerged oil has been mapped in the upper few meters of the water column (Brown et al., 2003b) allowing discrimination between submerged oil and phytoplankton in near surface waters.

More advanced approaches use a combination of LIF and absorption in the water Raman line. Specifically, oil thickness can be estimated from the reduction in the relative strength of the Raman line intensity and lab-based attenuation coefficients, while fluorescence provides for primary oil confirmation (Lennon et al., 2006). During a planned spill, comparison of thickness estimations from hyperspectral data

(400–1000 nm, 30-nm bandwidth) and the LIF Raman techniques showed qualitative agreement for very thin sheens (estimated to be 1–5  $\mu\text{m}$  thick). Yet, both the LIF and a combined hyperspectral/fluorescence volume underestimated the oil released by a factor of 2 and 5, respectively, and by a factor of ~10 for two further planned spills. LIF saturation for sheens thicker than 5 to 10  $\mu\text{m}$  or incorrect accounting for the oil's optical characteristics or sea conditions could explain the underestimate (Lennon et al., 2006).

### 3.2. Active remote sensing of the DWH

#### 3.2.1. Airborne Synthetic aperture radar remote sensing of the DWH

During the DWH spill, the UAVSAR instrument imaged 120,000  $\text{km}^2$  on 22–23 June 2010, collecting high-resolution radar along most of the U.S. Gulf coastline and over the main oil slick (Fig. 7E), including extensive coverage of the northeastern area of Barataria Bay, Louisiana where heavy oiling occurred (Jones & Davis, 2011; Jones et al., 2011). The average backscatter intensity from two UAVSAR swaths covering an area of ~15  $\times$  40 km within the main oil slick near the DWH rig site (Fig. 12A) showed oil slick returns that were significantly lower than returns from un-slicked water at the same incidence angle. UAVSAR returns show variations within the slick that apparently relate to oil thickness, fractional coverage, and/or oil emulsion characteristics. These returns are consistent with a non-uniform slick thickness, as verified with near-coincident, in situ, visual observations (Jones et al., 2011). The

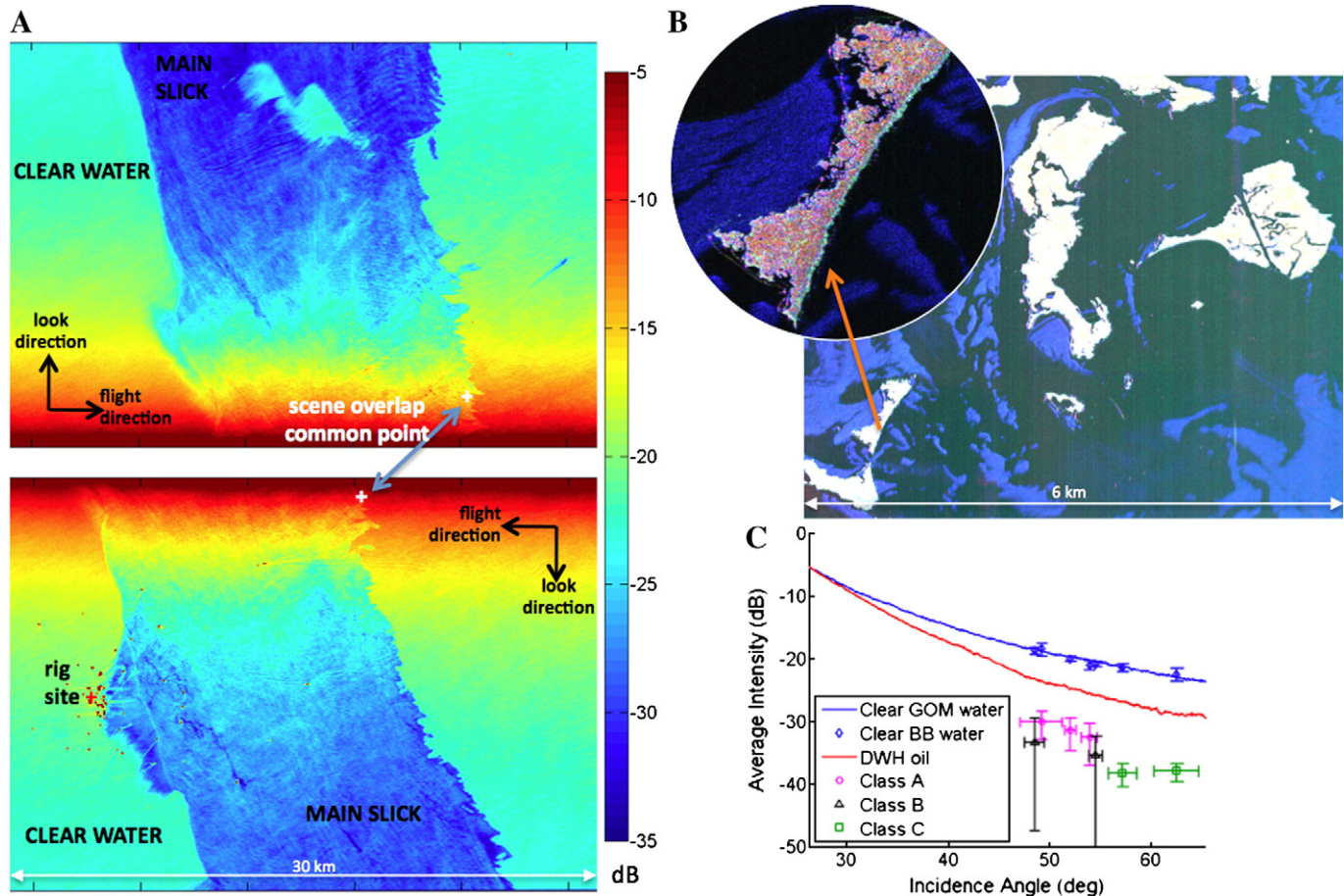


**Fig. 12.** A. UAVSAR radar backscatter intensity over the DWH spill site area from two adjacent tracks. Ships appear as dark red dots near the rig site in lower panel. Radar backscatter incidence angle dependency accounts for the general range dependent trends in look direction. B. UAVSAR multi-polarization radar backscatter intensity in northeastern Barataria Bay, Louisiana (red = HH, blue = VV, green = HV). Radar-dark areas in water areas show the oil sheen extent. Inset shows oiled vegetation along an island coastline in cross-polarization (green). C. Backscatter intensity versus incidence angle for clear water near the DWH rig site (solid blue line), within Barataria Bay (blue diamonds), and for main slick, oil-on-water areas near rig site (solid red line). Also shown are oil radar returns from Gulf side of Louisiana barrier islands at Barataria Bay entrance (Class A), within Barataria Bay just inland of the barrier islands (Class B), and in northeastern Barataria Bay, Bay Jimmy area (Class C). C adapted from Jones et al. (2011).

complex polarimetric data, i.e., the amplitude and phase of the backscatter signal for both horizontally and vertically polarized microwave radiation, also have been used to derive oil extent maps (Liu et al., 2011).

Minchew et al. (2012) studied in detail the L-band radar backscatter from the main oil slick near the wellhead location and calculated the co-polarized (HH and VV) and cross-polarized (HV) channels. In this notation, the first and second letters indicate transmit and receiving polarizations, respectively, of the microwave radiation. Results for areas with known oil slicks were compared to those for open water. The polarimetric analysis showed the scattering mechanism to be predominantly Bragg surface scattering in all areas of both unslicked sea surface and oil-slicked surface within the main slick over a range of incidence angles from 26° to 60°. In addition to the damping of the ocean wave spectral components by the oil, damping also results from an effective reduction of the ocean dielectric constant from a mixture of 65–90% oil with water in the surface layer. Note that measurement of the reduction in effective dielectric constant requires a relatively thick emulsified layer and is not measurable for thin oil sheens where the oil affects the radar backscatter only through alteration of the ocean wave spectra.

The high spatial resolution of the UAVSAR enabled the characterization of very near-shore oiling of vegetation in the marshlands affected by the DWH oil spill. The radar backscatter intensity for the different polarizations in the Bay Jimmy area to the northeast of Barataria Bay, Louisiana, showed evidence of surface oil slicks (Fig. 12B). These slicks, which a ground crew observed, were mainly sheen on the day of the UAVSAR overflight (Bruce A. Davis, NASA, Pers. Comm., 2010), and show up as radar-dark areas within the bay. Barataria Bay winds during the two days of data acquisitions were 2.5–5.0 m s<sup>-1</sup> and 2.5–3.5 m s<sup>-1</sup> from the southeast. UAVSAR returns from unslicked water in the Gulf and Barataria Bay were similar (Fig. 12C) and much higher than oil slick returns in either the main slick or Barataria Bay at all incidence angles. Furthermore, oil slick returns from the main slick were significantly higher than oil sheen returns in Barataria Bay, indicating sensitivity in the UAVSAR data to varying oil properties including thickness and weathering.

Minchew et al. (2012) and Jones et al. (2011) concluded that the L-band radar backscatter intensity is the most reliable radar indicator of oil slicks, affecting both co-polarized and cross-polarized channels. The largest variations within the oil slick related to the intensity and the anisotropy decomposition parameter (indicative of small-scale surface roughness), although measurement of the latter requires a low-noise instrument with cross-polarization capability, like the UAVSAR. This indicates that UAVSAR detection of varying oil slick characteristics (e.g., thickness, coverage, emulsification) requires a low instrument noise floor, which allows accurate measurement of cross-polarization return for oil slicks (Jones et al., 2011; Minchew et al., 2012).

### 3.2.2. Satellite synthetic aperture radar remote sensing of the DWH

Advantages of SSAR are their all-weather, day/night capabilities, higher spatial resolution than most other satellite sensors, and large spatial coverage. Disadvantages include many false positives and non-discrimination of thin sheens (0.1–1.0 μm) from thick oil requiring response actions. Thus, MODIS's poorer sensitivity to thin sheens was advantageous in better identifying where there was a non-negligible probability of finding thick oil. This difference is illustrated in Fig. 11B where the RadarSat-2 SAR area that appears slicked is significantly larger than the area in the MODIS image (Fig. 11A). Still, the prevalence of clouds meant that SSAR data often were very useful, particularly where cloudiness persisted for several days. Also, the detailed analysis of the polarimetric capabilities of ALOS PALSAR and RadarSat-2 has not yet been completed, which may potentially lead to detectable sensitivity related to thickness, analogous to that provided by the UAVSAR polarimetric analysis.

### 3.2.3. Airborne and spaceborne laser remote sensing of the DWH

#### 3.2.3.1. Laser bathymetry (lidar) submerged oil detection of the DWH.

Extensive airborne bathymetric lidar data were acquired during the DWH by the HSRL and CHARTS instruments, respectively (Fig. 7D, F, G), covering oil impacted areas in southeast Louisiana and over the spill in May 2010. Relevant CHARTS coastal data were collected for other areas prior to and following the DWH spill along the northern Gulf of Mexico as part of the U.S. Army Corps of Engineers, National Coastal Monitoring Program (Fig. 7G).

The CHARTS lidar mapped surface reflectance and identified structures likely associated with thicker oil slicks and likely sheens (Fig. 13A). Initial examination of water-column data showed evidence of unique lidar return backscatter properties that began near the location of surface oil slick features (i.e., green band, 532 nm). The spatial relationship between surface and subsurface features suggests oil injection. During this acquisition, winds were persistently easterly (66 to 88°) and light (3.9 and 5.0 m s<sup>-1</sup>) based on data from NOAA buoy 42040 (NOAA, 2010b), which would cause westerly surface oil advection. Comparison with the overview camera image sequence (Fig. 13E) shows that a largely contiguous slick line was abruptly disrupted (Fig. 13D, G). Moreover, the disrupted slick was associated with hazy patterns along an east-southeast/west-northwest trend (also see Fig. 13A). We propose that these data are consistent with a dispersant application along the trend of the hazy slick structures shortly prior. In the visual image of the disrupted slick area (Fig. 13D), the surface slick appears to remain only in two small patches, ~200 m apart. In this area (~100-m northeast of the green-red intersection in Fig. 13A), the lidar shows far more contiguous structures, which could be explained if some of the oil was slightly subsurface. Better understanding of the process underlying these observations may be provided from CASI data.

#### 3.2.3.2. Spaceborne lidar submerged oil detection of the DWH.

CALIOP also provides information on the presence of scatterers in the water column's upper ~40 m (Fig. 16C). In surface waters near the DWH site there was a significant increase in scatterers; however, other areas (e.g., near 26.7°N—not shown) also exhibit strong subsurface signals, too, although generally more spatially extensive. A strong subsurface feature at ~28.7°N was visible in many post-spill CALIOP data sets and was located near the DWH site. In some data sets, this feature's backscatter strength was far more strongly "peaked" than in Fig. 16F (e.g., 23 May and 8, 24 June 2010). This feature was not found commonly in pre-spill data. Because there are many non-oil, upper water-column scatterers, other data, such as AVIRIS, are required to relate CALIOP data positively to the DWH oil spill.

## 4. Oil spill impacts

### 4.1. Background: oil slick impact remote sensing

#### 4.1.1. Vegetation and ecosystem impacts

Petroleum hydrocarbons contain many toxic compounds that cause vegetation stress, changing leaf color and damaging the canopy. Longer-term, germination disruption and vegetation mortality can shift the ecosystem towards more chemically tolerant species, altering the dominant species (Li et al., 2005). Imaging spectroscopy has sufficient spectral resolution to characterize diagnostic absorption signatures (band position, width, depth, and symmetry) allowing monitoring of soil and vegetation changes. High spectral resolution is critical to enable discrimination between vegetation species and other scene items such as soil (Li et al., 2005).

Remote sensing provides the spatial coverage and sensitivity to assess oil spill damage and ecosystem impacts over statistically significant areas, provides data for logistically or politically inaccessible sites, and has been used for other disasters, but seldom for oil spills.

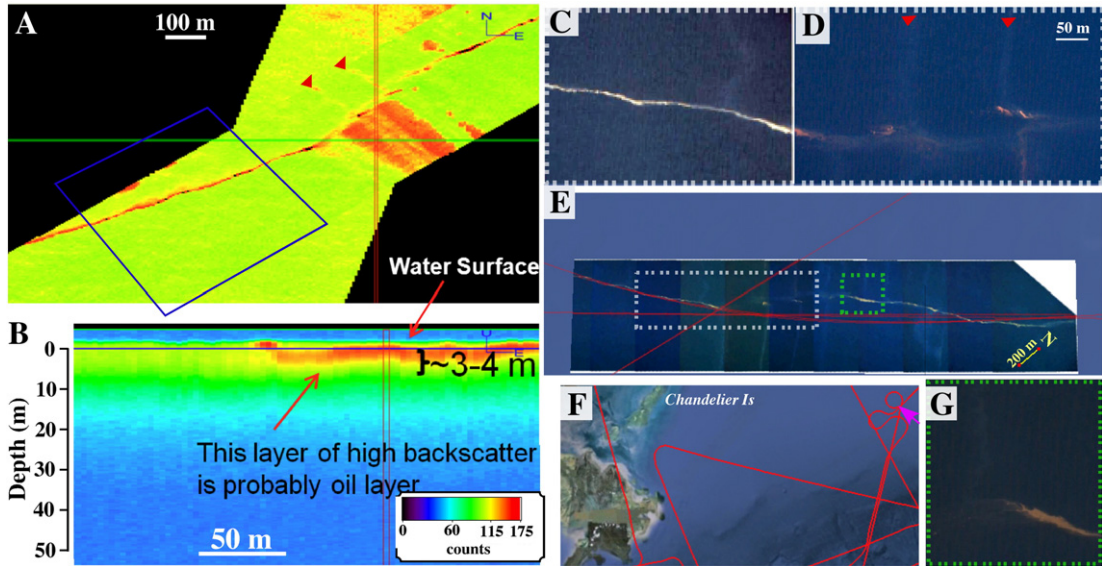


**Fig. 13.** A. Lidar-derived water column reflectance just below the sea surface from two flight lines. B. East–west cross-section of sea surface and water column backscatter. Green line in A indicates cross section location. Bright red and orange regions show evidence associated with oil submerged to 3 to 4-m deep. Lidar return scale on B. C and D. Contrast enhanced overflight images of area of where submerged scatterers were detected. E. Overview images along flight line showing location of images in C, D, and G. F. Location of crossing flightpaths in A indicated by arrow. G. Contrast enhanced image along flightpath.

Change detection and damage detection are two approaches to remote sense ecosystem oil spill impacts.

In change detection, changes in remote sensing parameters, such as surface reflectance, emittance, SAR backscatter, etc., identify changes such as ecosystem shifts. For example, soil property changes from the 1991 Kuwaiti oil spill for over 100 oil lakes were monitored with Landsat TM land surface temperature (LST) data (Husain & Amin, 1995). Areas with higher LST had either shallower or greater oil contamination than areas with lower LST, and gradually decreased over the 7-year study (Ud Din et al., 2008).

Plant stress can be identified by spectral shape changes including shifts towards shorter wavelengths of the “red edge,” located near 700 nm, due to chlorophyll loss and less scattering between leaves (Boochs et al., 1990). Although vegetation status often is assessed by the normalized difference vegetation index, spectral changes in the shape and location of the red edge are more robust (Li et al., 2005; van der Meijde et al., 2009). Spectral changes in the red edge have identified vegetation stress from petroleum hydrocarbons in ground-based spectrometer data (van der Meijde et al., 2009) and AVIRIS data for an oil spill in Jornada, New Mexico (Li et al., 2005). Because these variations can occur on sub-pixel scales, spectral mixture analysis often is used to characterize the fraction of endmembers (distinct components) in a pixel, such as dominant species (Roberts et al., 1998). SAR monitoring of canopy structural changes also can map plant stress effectively (Ramsey et al., 2011). Because other factors can cause vegetation stress, spatial information on vegetation oiling can be important (Li et al., 2005). Combining remote sensing oil hydrocarbon spectral detection (e.g., Fig. 4) with ecosystem stress remote sensing can allow discrimination between stresses from oil and other causes.

#### 4.1.2. Fire and oil spills

Oil spill response can involve accidental fire (Fingas, 2011) such as the 1979 Atlantic Sea Empress spill and the *Ixtoc-1* blowout, deliberate fire like the 1991 Gulf War oil spill, which involved ~625 deliberate well fires (Husain & Amin, 1995), or in situ burning as part of the spill response. In situ burns require a sufficiently thick oil slick for burning, >1 mm if the oil is un-emulsified although heavier crude oils can require a thicker layer (Fingas, 2011). Burning produces a semi-solid

tar-like layer or solid residues of ~5% the original volume (Fingas, 2011) that may sink after cooling (Buist, 2003). In situ burning is not a panacea; for many spills, weathering, logistics, weather, or proximity to populated areas restricts suitability. Yoshioka et al. (1999) concluded that 10–20% of historical spills could have been candidates for in situ burning. In situ burning advantages include very high and rapid oil removal rates, up to  $2000 \text{ m}^3 \text{ h}^{-1}$ , compared to other approaches, and short-term air pollution risk. Remote sensing data can provide guidance on where and when in situ burning is appropriate.

Burning oil is extremely hot, exceeding 700–800 °C, allowing mid-infrared (MIR)/TIR satellite monitoring through fire detection algorithms, which were used to monitor the uncontrolled 1991 Kuwait oil well fires (Fig. 14A) (Husain & Amin, 1995) and platform gas flaring (Elvidge et al., 2009). Well fires during the Iraqi withdrawal from Kuwait created the largest (non-accidental) spill in history, releasing an estimated 1–1.5 billion barrels of oil into more than 100 oil lakes covering 16 km<sup>2</sup>. Ultimately, these lakes contained 25–40 million barrels of oil. Oil fire identification and monitoring lasted over ~8 months using Landsat TM TIR (10,400–12,500 nm) and AVHRR MIR (3550–3950 nm) data, while AVHRR bands 3, 4, and 5 were used to map smoke plumes, which primarily were carbon soot (see Section 4.2). Well fire thermal emissions showed many continued burning at full strength after more than a month (Husain & Amin, 1995). MODIS also detected oil fires and plumes for the 2003 US–Iraq war (Fig. 14E).

#### 4.1.3. Oil spill fire aerosols

Remote sensing can track smoke plumes from in situ burns and well fires (Fig. 14). The Kuwait oil fires created extensive plumes that were tracked by geostationary and polar orbiting satellites (Fig. 14A) in support of air-sampling missions (Ferek et al., 1992). For example, data documented the relatively narrow width of the plumes (20–50 km) over hundreds of kilometers (Fig. 14B). Comparison of plume drift with winds at different heights was used to infer plume altitudes from satellite data (Limaye et al., 1992).

#### 4.1.4. Oil slick volatiles

Volatile organic hydrocarbons from oil spills, present significant health concerns and create pollutants like ozone and nitrous oxides

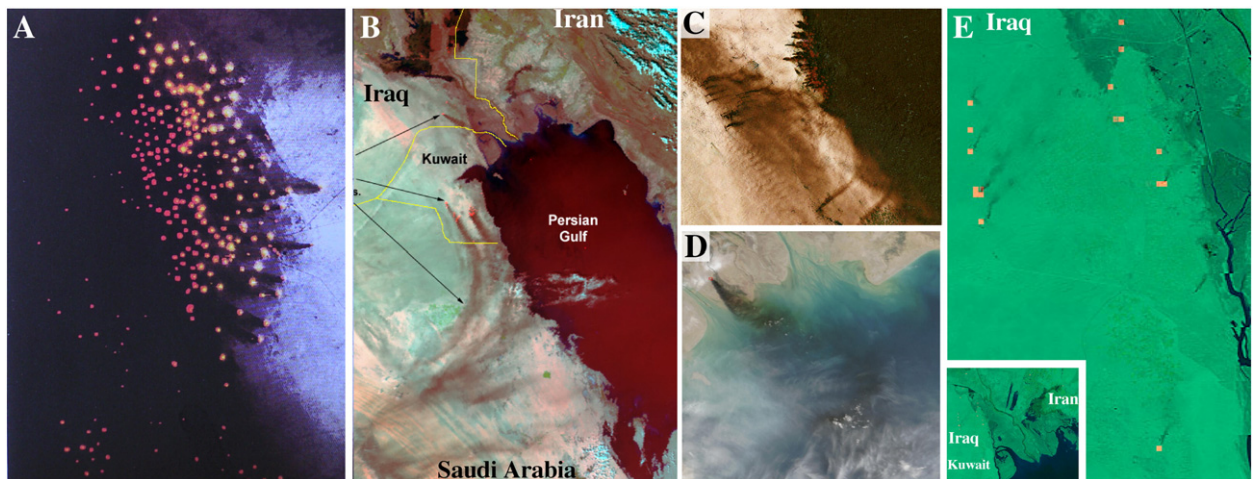


**Fig. 14.** A. NOAA AVHRR satellite image of 1991 Kuwait oil fires (Husain and Amin 1995). B. Multispectral, false color image ( $\text{RGB} = 3.74, 0.86, 0.63 \mu\text{m}$ ), of 1991 Kuwait oil fires and smoke on 12 Feb. 1991 (NOAA 1991). C. True color, Landsat 5 TM image of 1991 Kuwait oil fires and smoke on 23 Feb. 1991 (NASA 1991). D. MODIS image of pipeline rupture and ignition and smoke plume (NASA 2004). E. MODIS false color image ( $\text{RGB} = 3.96, 0.86, 0.645 \mu\text{m}$ ) of 2003 S. Iraq oil fires and smoke on 12 Mar. 1991, (NOAA 2003). Red pixels show positive fire detection. (For interpretation of the references to color in this figure legend, the reader is referred to the web version of this article.)

( $\text{NO}_x$ ), which remote sensing can detect, providing important early warnings. For the Kuwaiti oil fires,  $\text{CO}_2$  emissions were large, with airborne measurements indicating  $4.9 \times 10^5$  tonnes  $\text{CO}_2$ /day (Hobbs & Radke, 1992), an amount that would be detectable by current satellite instruments such as GOSAT. Because crude oil often contains sulfur, combustion can produce significant sulfur dioxide,  $\text{SO}_2$ . For the Kuwait oil fires, daily  $\text{SO}_2$  emissions were estimated at 20,000 to 22,500 t (Husain & Amin, 1995). Current spaceborne instruments can observe some trace gases, for example; SCIAMACHY can detect  $\text{CO}_2$  and  $\text{SO}_2$  (Burrows et al., 2011). Nevertheless, spill-related

pollution can be difficult to discriminate from other anthropogenic pollution sources, particularly where the instrument footprint is large ( $30 \times 240 \text{ km}$  footprint for SCIAMACHY).

Airborne remote sensing can play a role in disaster response by detection of dangerous or toxic gas concentrations. A wide range of gases can be identified from both MIR and TIR spectral signatures using a spectral library matching approach (Kroutil et al., 2011), although high spectral resolution data such as from Fourier Transform InfraRed (FTIR) spectrometers are critical (Kroutil et al., 2011).

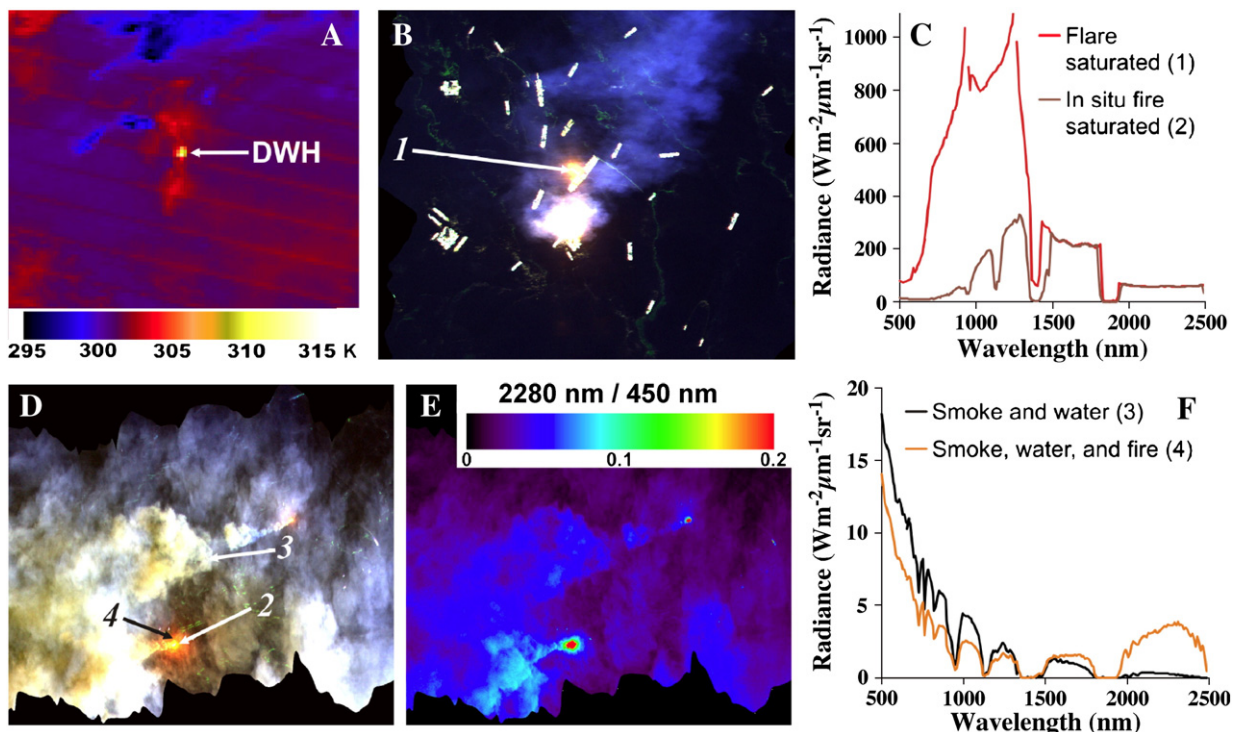


**Fig. 15.** A. Mid infrared, 4- $\mu\text{m}$  brightness temperature for a daytime MODIS Terra image acquired at  $\sim 1700$  UTC 9 July 2010 ( $\sim 100 \text{ km}$  field of view). Flaring from the DWH well site resulted in the elevated brightness temperatures in the center of the image. B. AVIRIS false color composite ( $\text{RGB} = 2277, 1682, 724 \text{ nm}$ ) of DWH well site, acquired  $\sim 1510$  UTC, 9 July 2010. Flaring is from two ships in the image center. C. Radiance spectra from AVIRIS images in B for an extremely saturated pixel from the center of the smaller flare, and in D for a less saturated spectrum from an in situ fire. D. AVIRIS false color composite (same RGB bands as B) showing in situ burning acquired  $\sim 2235$  UTC, 9 July 2010. E. Band ratio image showing fire detection over water. F. AVIRIS radiance spectra from pixels in D.

## 4.2. Oil slick ecosystem impact remote sensing of the DWH

### 4.2.1. In situ burning and well flaring

In situ burning was used widely (411 burns) during the DWH spill, consuming  $4.5 \times 10^7$  L of oil (Lehr et al., 2010). Elevated brightness temperatures were evident in multiple MODIS scenes during the spill (Fig. 15A). Warmer areas corresponded with MODIS visible indication of thick oil where in situ burning would be more likely. However, increased brightness temperatures stayed close to background brightness temperatures and did not exceed the 37 °C threshold used for MODIS daytime fire detection (Giglio et al., 2003). Only the pixel containing flaring at the DWH well site resulted in an obvious fire detection based on elevated brightness temperature (Fig. 15A), in part because in situ burning covered a very small fraction of a MODIS pixel.

The finer spatial resolution of airborne remote sensing provides significant advantages for monitoring in situ burns, although sensor saturation is much more likely. An extreme example of saturation is in the 3.4-m AVIRIS data acquired over the DWH well site (Fig. 15B).

Flares cause saturation through much of AVIRIS's spectral range, in some cases, saturating a majority of AVIRIS NIR bands (Fig. 15C). Blackbody emission curves were fit to the unsaturated bands of flare spectra, indicating temperatures potentially in excess of 1700 °C. Smoke cover was a dominant feature in AVIRIS images acquired over in situ fires. Smoke absorption greatly reduced emitted fire radiance at wavelengths shorter than 1200 nm, but minimally attenuated emitted radiance at longer wavelengths. Due to the low reflectance of solar irradiance by water and smoke, fires were easily detectable using a ratio of the 2280 and 450 nm bands (Fig. 15E). Fire increases the 2280-nm band radiance (Dennison & Roberts, 2009), thereby increasing the band ratio above 0.2. A fire temperature retrieval algorithm (Dennison & Matheson, 2011) fit to AVIRIS spectra acquired over an in situ burn found effective temperatures of up to 1025 °C.

Fires from in situ DWH burns produced smoke plumes (Fig. 15D) that were characterized by the CALIOP lidar on 10 July 2010. Records show in situ burning on both 9 and 10 July (Lehr et al., 2010). On 10 July CALIOP recorded an aerosol layer rapidly rising to ~2 km altitude

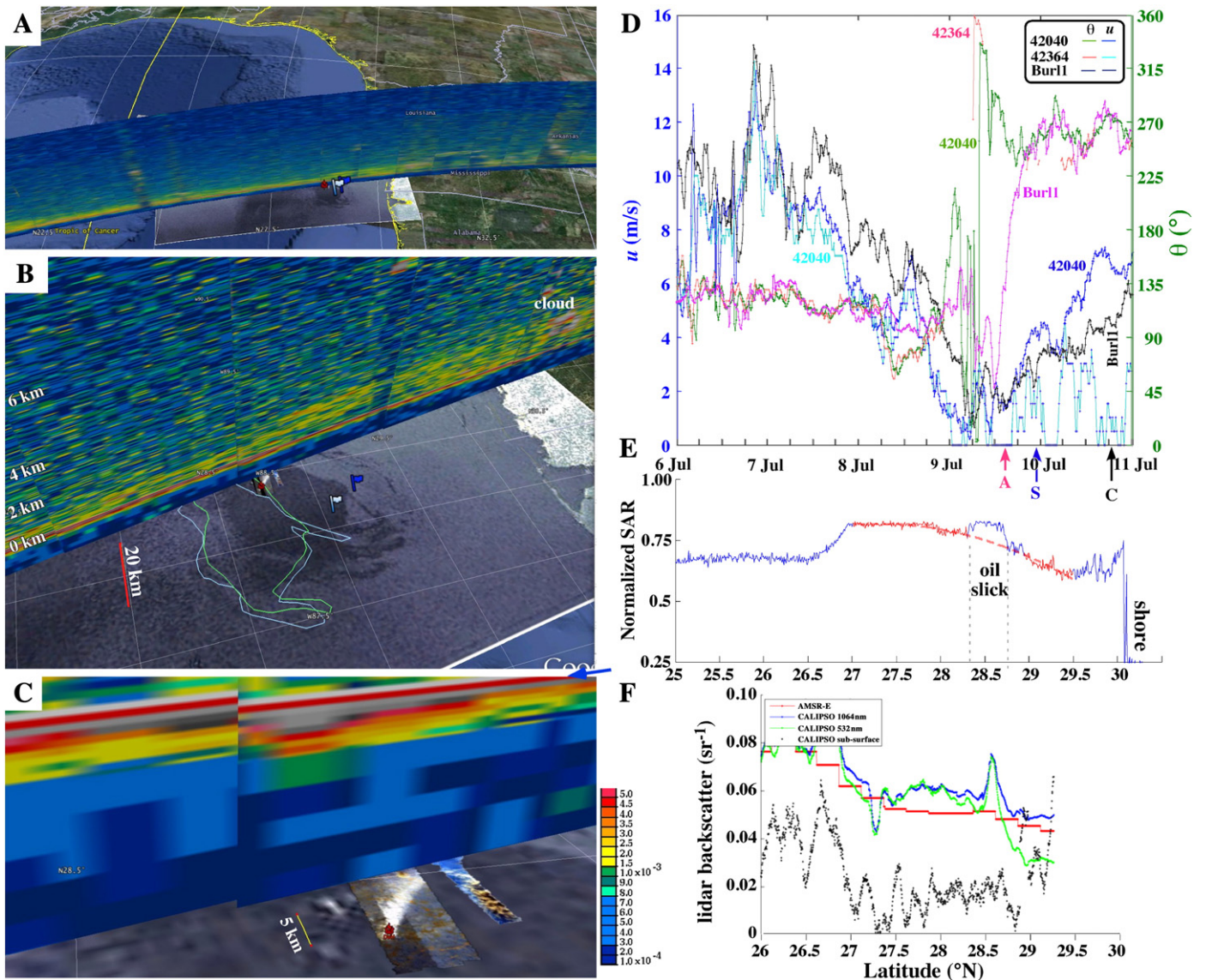


**Fig. 16.** A–C. CALIPSO LIDAR, Radarsat 1 SAR, and AVIRIS data for (1854 UTC) 10 July; (2341 UTC) 9 July, 23:41; and (1530 UTC) 9 July, respectively. Size scale on B and C. B. Slick outlines from SAR image for (0343 UTC) and (1158 UTC) 11 July from ASAR, and CosmoSkyMed2, respectively. D. Wind speed,  $u$ , and direction for three meteorology stations, 42040 and 42364 (on B), and Burl1. Time of CALIPSO, and Radarsat1 overpasses and AVIRIS flights indicated (C, S, and A, respectively). E. Normalized, mean SAR return for 18-pixel wide swath along CALIPSO track, and second order polynomial fit (red) to non-slick pixels (red). F. CALIPSO LIDAR backscatter for 532 nm and 1064 nm, subsurface return, and modeled sea surface backscatter for the Gulf of Mexico. Data key on panel.

near the incident site that was consistent with smoke. The aerosol layer gradually thickened towards land, leading to cloud formation ~10 km north of the shoreline (Fig. 16B).

This CALIPSO satellite overpass was during a period of persistent calm to light (0–5 m s<sup>−1</sup>) WSW winds (Fig. 16D) and followed AVIRIS flights on 9 July (1530 UTC) at the incident site that showed a strong smoke plume spreading WNW (Fig. 16). Smoke advection in the 9 July AVIRIS scene was most consistent with ESE winds at the Burl1 weather station, located at East Pass, Louisiana (28.905°N, 89.43°W). Such light winds generally imply minimal surface slick advection, explaining the good relationship between a 10 July RadarSat1 SAR image and CALIPSO backscatter (Fig. 16F). SAR images from 11 July showed a similar shaped oil slick outline near the DWH incident site, shifted ~10–15 km further south (see outlines in Fig. 16B, blue—ASAR 0343 UTC 11 July, green—CosmosSkyMed2, 1158 UTC, 11 July).

#### 4.2.2. Oil slick trace gases remote sensing of the DWH

The airborne ASPECT sensor suite includes a FTIR spectrometer for trace gas identification based on MIR and TIR spectral signatures from high spectral-resolution, along-track data. Using an extensive spectral library, trace gases with column abundances in the ppm-meter range can be identified through a multiple linear regression analysis through a trained filter. ASPECT flies at a low altitude, 1000 m, decreasing the effect of atmospheric temperature profiles on the signatures.

ASPECT data were obtained during 86 repeat DWH overflights that included coverage of in situ burns and the spill site (Fig. 7H). TIR data allowed positive detection of CO<sub>2</sub>, CO, and methanol while acetaldehyde was detected in the MIR (3660 nm). Other pollutants were below system detection levels. The methanol feature was located persistently within 1.5 km of the well site and was interpreted as methanol evaporation from rising fluids from the well cap. Methanol was injected into the well cap to reduce hydrate formation; however, significant oil, gas, and methanol escaped the cap (Kroutil et al., 2011).

#### 4.3. Vegetation and ecosystem impacts remote sensing of the DWH

Extensive AVIRIS data for the DWH spill (Fig. 7A) were collected, including pre-oil inundation of the entire Gulf coast and are being analyzed to identify previously stressed ecosystems and derive dominant species in conjunction with ground reference observations and to identify oiled vegetation based on its spectral signature (Kokaly et al., 2010). These data are essential for interpreting post-oil spill effects and can aid resource allocation and remediation efforts by directing resources to the more resilient portions of the coastal ecosystem. Analysis of HICO DWH data (Sonia Gallegos, Naval Research Laboratory, Pers. Comm., 2011) in conjunction with MODIS and Landsat data will aid in extending AVIRIS ecosystem data.

Radar backscatter from vegetation relates to the physical structure and dielectric properties of the backscatter media, including canopy structure. The UAVSAR results for oil-affected wetlands (Fig. 12B) in Barataria Bay show both a sensitivity to oiled vegetation and the potential for L-band radar's use in measuring oil on the soil or lower canopy in areas where the upper canopy is not directly oiled (Jones et al., 2011; Ramsey et al., 2011). For example, the UAVSAR radar detected the signature of oiled vegetation on the windward (SE) side of a Bay Jimmy Island but not on the leeward side (Fig. 12B, inset), a result consistent with true color images of the area (Jones et al., 2011). The oil-impacted shoreline exhibited higher cross-polarization (HV) returns relative to the co-polarized (HH and VV) returns (green band in Fig. 12B). This oiled shoreline signature was observed throughout northeastern Barataria Bay (Ramsey et al., 2011), where DWH oil impacts were among the highest in May and June 2010. These results show that high resolution UAVSAR data can complement AVIRIS hyperspectral data to improve detection of impacted areas earlier and to characterize more fully the impacts.

## 5. Discussion

### 5.1. Oil slick remote sensing

In the DWH response, remote sensing aided efforts to address a key question: How much oil was on the sea surface? AVIRIS demonstrated a method to estimate quantitatively oil slick thickness, but could only cover less than a third of the slick at best. Thus, total slick estimates used MODIS data to scale the AVIRIS-derived oil quantities (Clark et al., 2010). Unfortunately, synergistic AVIRIS and MODIS data only were available on a few days due to cloud cover, technical problems, etc. Both MODIS and SSAR data were useful for response flight planning, particularly for finding oil slick locations that were poorly predicted and for identifying oil movements towards coastal ecosystems. However, the limited ability of satellite data to discriminate thick oil slicks from thin oil sheens prevented their playing a more direct role.

For the foreseeable future, remote sensing most likely will augment rather than replace experienced airborne observers for several reasons. First, each oil spill is unique, preventing easy application of remote sensing without significant human interpretation, and second direct visual airborne observations can provide insights and opportunistic observations of the oil spill over a wider range of conditions. Still, remote sensing can address the shortage of experienced observers within the high operational pace demanded by large-scale oil spills and also reduce observer biases. Approaches such as NIR imaging spectroscopy that require significant computation face challenges to translation into Rapid Response Products; however, computer improvements promise improved integration into future robust oil spill response.

#### 5.1.1. Passive airborne oil slick remote sensing

As noted, because an oil slick's visible appearance depends far more strongly on the oil-to-water emulsion ratio and air content than to thickness, hyperspectral visible reflectance approaches that neglect emulsion levels are not robust. Moreover, passive visible observations are susceptible to false oil detection. In contrast, oil thickness measurements using NIR C–H absorption features were found robust from 0.1 to 20 mm. Critical to AVIRIS's success was its high signal to noise ratio and fine (10-nm) spectral resolution; sensors with poorer performance would make the spectral library approach far less likely to estimate the correct thickness. Currently, a spectral library is needed for each oil, i.e., an oil sample is required. Further study could enable derivation of the "spectral library" from known or assumed oil properties.

TIR oil detection is far more susceptible to false positives than visible slick detection, sharing similar problems from sea state dependence, cloud interference, and difficulty in discriminating from other sea surface features, as well as sea-surface thermal variations and temperature-profile dependent atmospheric correction. Current airborne and satellite TIR only provide loose discrimination between thin slicks and very thin oil sheens (Grierson, 1998). Thus, awaiting daylight and passive reflective imagery is often more practical. One advantage of airborne TIR is that clouds above the airplane are far colder and have lower emissivity and thus, do not interfere with airborne TIR remote sensing data under cloudy skies.

Although airborne TIR remote sensing has focused on oil identification from thermal signatures, hyperspectral TIR data has the potential to derive quantitative oil slick thickness using an approach similar to that used for NIR imaging spectroscopic data. Furthermore, lab spectra suggest that some of these features can discriminate between oil types (Byfield, 1998). However, as with NIR spectral features, TIR oil emissivity depends on oil–water emulsions (Salisbury et al., 1993). Significant work is needed to address complexities from atmospheric corrections, which must consider relevant emissions and absorptions for the thermal profile.

Usually, hyperspectral TIR data are analyzed with an in-scene atmospheric compensation algorithm that uses only the data itself without recourse to ancillary atmospheric data or models (Young et al., 2002). Data then are searched for spectral features of interest using generalized least-squares regression on a spectral covariance matrix derived from the data.

An alternate TIR approach with the potential to indicate oil thickness is Apparent Thermal Inertia, ATI. If the oil and seawater properties (the latter is sea state dependent) are known, then the sea surface's thermal lag relates in some predictable manner to oil slick thickness (Asanuma et al., 1986). However, ATI derivation likely is complicated by the oil slick's changing properties, including the oil-to-water emulsion ratio, which affects slick emissivity (Salisbury et al., 1993).

### 5.1.2. Passive satellite oil slick remote sensing

Current passive satellite approaches suffer from false identification, infrequent overpasses, coarse spatial resolution, cloudiness sensitivity, and limited ability to distinguish between biogenic sheens, oil sheens, and thick oil slicks and that are thousands of times thicker. Multiple satellites now allow for repeat data on one to several day time-scales (clouds permitting). However, significant oil advection can occur during this revisit time, reducing satellite data utility, given the need for timely resource allocation. Further, analysis approaches that assume all spectral features are either sea surface or oil, e.g., Chen and Chang (2010) are incorrect, leading to false positives and potential resource misallocation and thus, are not useful for spill response. As a result, satellite data largely plays a support role, guiding airborne and surface observers.

The success of AVIRIS quantitative oil spill thickness mapping suggests that the proposed Hyperspectral InfraRed Imager (HyspIRI) satellite mission could similarly aid oil spill response. HyspIRI is a Tier 2, NRC earth decadal survey satellite that will provide 60-m data in 210 channels from 380 to 2500 nm and 8 channels from 4 to 12  $\mu\text{m}$  with 145 and 600-km swaths, respectively, with a planned 3-day revisit utilizing sensor pointing (HyspIRI, 2011).

### 5.1.3. Active satellite and airborne oil slick remote sensing

The most common active oil spill remote sensing approach is all weather SSAR. Marine slicks are detectable for wind speeds from 2–3 to 10  $\text{m s}^{-1}$  for incidence angle range from 20° to 45°, with an optimum wind speed range from 3.5 to 7.0  $\text{m s}^{-1}$  (Garcia-Pineda et al., 2009). SSAR's numerous false positives are a drawback and it generally only provides a binary indication of slick extent, providing little useful response guidance. Such data are of minimal use for improving oil spill models as they largely represent advection of thin sheen areas, rather than the thick oil that contains most of the volume (Hollinger & Mennella, 1973). In a spill response, the primary remote sensing objective is not to find sheens, but to identify thick oil, particularly as it approaches coastal ecosystems, and also outside the spatial envelope where oil was believed to exist. SSAR primarily supported these goals by guiding surveillance flights on multiple cloudy days when MODIS data were unavailable.

Due to its higher sensitivity than SSAR, the UAVSAR data showed a relationship to oil slick characteristics such as thickness, emulsification, and coverage. The underlying mechanism is Bragg scattering from a layer with the dielectric properties of a mixture of oil and water (Minchew et al., 2012). Observed radar backscatter variations within the slick relate to varying sea-surface dielectric characteristics due to different oil slick compositions, emulsion levels, and to variable oil modification of the short-wavelength ocean wave field. UAVSAR data showed that a low noise, fully polarimetric radar instrument can differentiate between different oil slick properties to a greater level than earlier airborne SAR or SSAR. These results support controlled studies to separate the effects of thickness, surface coverage, and oil properties on the radar backscatter, which could provide an oil remote sensing tool for cloudy and night conditions.

LIF allows discrimination between oil and non-oil slicks, preventing false positives, but, in a planned oil release study, LIF underestimated total oil by factors of 2 to 5 (Lennon et al., 2006). Several factors could have confounded the analysis including unresolved heterogeneity, atmospheric corrections, and sea state and upper ocean optics, and chemical weathering changes. Although, LIF approaches largely are appropriate to very thin sheens, the majority of the oil lies in the thick oil slicks. Thus, LIF poorly matched DWH needs.

Airborne bathymetric lidar and spaceborne lidar both demonstrated an exciting new capability to remote sense near-surface, submerged oil. Development of an operational lidar technology will provide much needed field data to understand oil spill processes better related to oil dispersion and shallow sub-surface oil.

### 5.2. Applications of quantitative oil slick thickness mapping

Oil remote sensing can improve our understanding of natural marine hydrocarbon seepage (Washburn et al., 2005), assess vessel operations and spill inputs, and improve oil spill science (Adamo et al., 2009). Quantitative oil thickness mapping will allow true mass transport determination, rather than slick pattern advection or sheen advection, improving oil spill advection and emulsification models. Cheng et al. (2010), showed the need for modeling improvements from repeat SSAR data despite a lack of SSAR thickness information.

### 5.3. Real world application of remote sensing technology to oil slicks

Clearly the appropriate time for developing new oil spill remote sensing approaches is not during the response, when the main goal is mitigating damage. During a response, there is a strong bias to allocate response resources based on proven and widely accepted, i.e., defensible, technologies because time is unavailable to evaluate a technology's accuracy or applicability. The transition to operational readiness from a lab or field demonstrated technology, much less from a theoretical technology, is significant. Many steps are required to validate technology in the appropriate environment, including integration with critical hardware and analysis software before reaching operational technology readiness (Ramirez-Marquez & Sauser, 2009).

Technologies with proven and accessible Rapid Response Products, like MODIS, are far more likely to contribute to spill response. Data fusion of ancillary data such as meteorology can be highly helpful; however, data coordination logistics during a spill are challenging.

Oil spills provide an opportunity to field test new approaches under real world conditions (Clark et al., 2010), as does the post-spill period for monitoring technologies (Ud Din et al., 2008). Although oil spills occur frequently, they are unpredictable and highly challenging for data collection mobilization, particularly for small oil spills.

Large spills present a more feasible target; however, careful calibration/validation studies may be impossible during oil spills. A key step in most remote sensing applications is field validation, which generally requires a planned release. Although large test facilities can play a role, they cannot recreate many real-world characteristics of a marine oil spill from a remote sensing perspective. In this regard, natural marine hydrocarbon seeps provide real world oil slicks for studying oil slick processes (Leifer et al., 2006) without release permits.

In the DWH response, field-testing of the NIR approach was approved because of its prior success with oil slicks in AVIRIS Katrina data (Swayze et al., 2007), physics-based mechanism, and lab studies. Furthermore, spatial patterns in the derived oil-thickness maps (Fig. 9) were consistent with oil slick processes; key to confidence in the approach. Symmetric oil thickness (e.g., Fig. 8) would have necessitated more detailed validation data, as for the Ocean Imaging system in the Coal Oil Point seep field (Svejkovsky et al., 2009). Thus, evaluation of a remote sensing approach must demonstrate consistency with oil slick

processes (Fig. 1) in the marine environment under real world conditions (water vapor, waves, winds, platform vibration, etc.).

Where multiple sensors provided overlapping data, significant benefit was gained in interpretation, such as AVIRIS and CALIPSO, or AVIRIS and MODIS. However, other attempted synergistic data collections, such as UAVSAR and AVIRIS were thwarted by logistics. Thus, best oil spill response would involve an operational readiness for multiple sensor integration such that logistical details are not bottlenecks, of which ASPECT is an example.

Some technologies played a minor role in the DWH spill response because they lacked a reliable track record, a well-understood underlying physical mechanism, a Rapid Response Product, significant contribution beyond other approaches, or largely were mismatched with primary response needs of thick oil mapping. The extensive DWH remote sensing data should be analyzed to enable improvement of new and existing remote sensing technologies.

## 6. Conclusions

New remote sensing technologies and techniques were developed during the first decade of the 21st century and were used during the *Deepwater Horizon* spill. Actively supporting the response were the MODIS and MERIS visible satellite sensors, and to a lesser extent satellite SAR. Airborne remote sensing platforms also were important including multispectral expert systems, hyperspectral airborne sensors, ultrasensitive L-band airborne radar, and airborne thermal infrared spectrometers. Particularly important was the development of the AVIRIS hyperspectral approach to quantify oil thickness, a previously unobtainable achievement with revolutionary potential for oil spill science.

Technology incorporation into oil spill response requires strong confidence in robustness and reliability. Rapid Response Products, such as the Ocean Imaging expert system and MODIS satellite data were critical for the timely response needs to support decision-making. Promising technologies without a rapid response capability largely were not useful during the spill, although important data clearly were collected for post-spill interpretation.

Oil spills present rare field test opportunities for new technologies, in part, because planned releases are difficult to permit and consequently are rare. The need for increased and long-term oil spill science research clearly was demonstrated during the *Deepwater Horizon* spill—the appropriate time for developing new oil spill remote sensing technology is not during a spill response. A paradigm shift in oil spill research is critical to move technologies from the research and theoretical levels to operational readiness prior to the next large oil spill.

## Acknowledgments

We thank the important role and support of NASA, NOAA, NSF, and USGS in the development of these technologies. Some of the research described herein was carried out in part at the Jet Propulsion Laboratory, California Institute of Technology, under a contract with the National Aeronautics and Space Administration. Development of the multispectral rapid response thickness sensor by Ocean Imaging was supported by the Bureau of Ocean Energy Management, Regulation, and Enforcement (BOEMRE) under contract M07PC13205. NSF support enabled the SEBASS data collection. The efforts of Susan Ustin (UC Davis) and Raymond Kokaly (USGS) for ecosystem data collection and analysis and David Tratt for editing are thanked.

### Disclaimer

The views and conclusions expressed in this article are those of the authors and do not necessarily represent the views of the Universities, NASA, and NOAA. Further, any use of trade, product, or firm names is for descriptive purposes only and does not imply endorsement by the U.S. Government.

## References

Adamo, M., De Carolis, G., De Pasquale, V., & Pasquariello, G. (2009). Detection and tracking of oil slicks on sun-glittered visible and near infrared satellite imagery. *International Journal of Remote Sensing*, 30, 6403–6427.

Albaiges, J., Morales-Nin, B., & Vilas, F. (2006). The Prestige oil spill: A scientific response. *Marine Pollution Bulletin*, 53, 205–207.

Asanuma, I., Muneyama, K., Sasaki, Y., et al. (1986). Satellite thermal observation of oil slicks on the Persian Gulf. *Remote Sensing of Environment*, 19, 171–186.

ASCE (1996). State of the art review of modeling transport and fate of oil spill (Task Committee on Modeling Oil Spills of the Water Resources Engineering Division). *Journal of Hydraulic Engineering*, 122, 594–609.

ASTM (1996). Standard guide for visually estimating oil spill thickness on water. *ASTM International, Report Number F2534-06* (pp. 4). <http://dx.doi.org/10.1520/F2534-06>.

Bentz, C., & Pellen de Miranda, F. (2001). Application of remote sensing data for oil spill monitoring in the Guanabara Bay, Rio de Janeiro, Brazil. *International Geoscience and Remote Sensing Symposium, 2001. IGARSS '01* (pp. 333–335). Sydney, Australia: IEEE.

Bonn Agreement (2004). *Bonn agreement aerial surveillance handbook* (pp. 96).

Bonn Agreement (2009). *Bonn agreement aerial surveillance handbook* (pp. 106).

Boochs, F., Kupfer, G., Dockter, K., & Kühbauch, W. (1990). Shape of the red edge as vitality indicator for plants. *International Journal of Remote Sensing*, 11, 1741–1753.

Boström, C.-E., Gerde, P., Hanberg, A., et al. (2002). Cancer risk assessment, indicators, and guidelines for polycyclic aromatic hydrocarbons in the ambient air. *Environmental Health Perspectives*, 110, 451–488.

Bradley, E. S., Roberts, D. A., Dennison, P. E., et al. (2011). Google earth and Google fusion tables in support of time-critical collaboration: Mapping the deepwater horizon oil spill with the AVIRIS airborne spectrometer. *Earth Science Informatics*, 4, 169–179.

Brekke, C., & Solberg, A. H. S. (2005). Oil spill detection by satellite remote sensing. *Remote Sensing of Environment*, 95, 1–13.

Brown, C. E. (2011). Laser fluorosensors. *Oil spill science and technology* (pp. 171–184). Boston: Gulf Professional Publishing.

Brown, C., Fingas, M., & Hawkins, R. (2003). Synthetic aperture radar sensors: Viable for marine oil spill response. *26th Arctic and Marine Oil Spill Program (AMOP) Technical Seminar*. Victoria, Canada: Environment Canada.

Brown, C. E., Marois, R., Myslicki, G. E., et al. (2003). Remote detection of submerged oil slicks with a range-gated laser fluorosensor. *Proceedings of the 2003 International Oil Spill Conference* (pp. 1–6). Vancouver, British Columbia: EIS Digital Publishing.

Buist, I. (2003). Window-of-opportunity for in situ burning. *Spill Science & Technology Bulletin*, 8, 341–346.

Burrows, J. P., Goede, A. P. H., Muller, C., & Bovensmann, H. (2011). SCIAMACHY—Exploring the changing Earth's atmosphere. In G. Manfred, & H. Bovensmann (Eds.), (1st ed.). Springer.

Byfield, V. (1998). *Optical remote sensing of oil in the marine environment*. (pp. 302). Ph.D. Thesis, School of Ocean and Earth Science, University of Southampton, Southampton, UK.

Byfield, V., & Boxall, S. R. (1999). Thickness estimates and classification of surface oil using passive sensing at visible and near-infrared wavelengths. *Geoscience and Remote Sensing Symposium, 1999. IGARSS '99 Proceedings. IEEE 1999 International* (pp. 1475–1477). : IEEE.

Cai, G., Huang, X., Du, M., & Liu, Y. (2011). Detection of natural oil seeps signature from SST and ATI in South Yellow Sea combining ASTER and MODIS data. *International Journal of Remote Sensing*, 31, 4869–4885.

Carrera, P., Churnside, J. H., Boyra, G., Marques, V., et al. (2006). Comparison of airborne lidar with echosounders: A case study in the coastal Atlantic waters of southern Europe. *ICES Journal of Marine Science: Journal du Conseil*, 63, 1736–1750.

Chen, C.-F., & Chang, L.-Y. (2010). Extraction of oil slicks on the sea surface from optical satellite images by using an anomaly detection technique. *Journal of Applied Remote Sensing*, 4, 043565.

Cheng, Y., Li, X., Xu, Q., Garcia-Pineda, O., Andersen, O. B., & Pichel, W. G. (2010). SAR observation and model tracking of an oil spill event in coastal waters. *Marine Pollution Bulletin*, 62, 350–363.

Chust, G., & Sagarminaga, Y. (2007). The multi-angle view of MISR detects oil slicks under sun glitter conditions. *Remote Sensing of Environment*, 107, 232–239.

Clark, R. N. (1999). Spectroscopy of rocks and minerals, and principles of spectroscopy. In A. N. Rencz (Ed.), *Manual of Remote Sensing, Remote Sensing for the Earth Sciences* (pp. 3–58). New York: John Wiley and Sons.

Clark, R. N., Curchin, J. M., Hoefen, T. M., & Swayze, G. A. (2009). Reflectance spectroscopy of organic compounds: 1. Alkanes. *Journal of Geophysical Research*, 114, E03001.

Clark, R. N., Swayze, G. A., Leifer, I., et al. (2010). A method for quantitative mapping of thick oil spills using imaging spectroscopy. *U.S. Geological Survey Open-File Report Number 2010-1167* (pp. 51).

Clark, R. N., Swayze, G. A., Livo, K. E., et al. (2003). Imaging spectroscopy: Earth and planetary remote sensing with the USGS Tetracorder and expert systems. *Journal of Geophysical Research*, 108(E12).

Cunliffe, M., & Murrell, J. C. (2009). The sea-surface microlayer is a gelatinous biofilm. *International Society for Microbiology Ecology Journal*, 3, 1001–1003.

Dennison, P. E., & Matheson, D. S. (2011). Comparison of fire temperature and fractional area modeled from SWIR, MIR, and TIR multispectral and SWIR hyperspectral airborne data. *Remote Sensing of Environment*, 115, 876–886.

Dennison, P. E., & Roberts, D. A. (2009). Daytime fire detection using airborne hyperspectral data. *Remote Sensing of Environment*, 113, 1646–1657.

DiGiacomo, P. M., Washburn, L., Holt, B., & Jones, B. H. (2004). Coastal pollution hazards in southern California observed by SAR imagery: Stormwater plumes, wastewater plumes, and natural hydrocarbon seeps. *Marine Pollution Bulletin*, 49, 1013–1024.

Donelan, M. A., & Pierson, W. J. (1987). Radar scattering and equilibrium ranges in wind-generated waves with application to scatterometry. *Journal of Geophysical Research*, 92(C5), 4971–5029.

Elvidge, C., Ziskin, D., Baugh, K., et al. (2009). A fifteen year record of global natural gas flaring derived from satellite data. *Energies*, 2, 595–622.

Espedal, H. A. (1999). Satellite SAR oil spill detection using wind history information. *International Journal of Remote Sensing*, 20, 49–65.

Farmer, D., & Li, M. (1994). Oil dispersion by turbulence and coherent circulations. *Ocean Engineering*, 21, 575–586.

Fay, J. A. (1971). The spread of oil slicks on a calm sea. In D. P. Hoult (Ed.), *Oil on the sea: Proceedings of a symposium on the scientific and engineering aspects of oil pollution of the sea* (pp. 53–63). New York, NY: Plenum Press.

Ferek, R. J., Hobbs, P. V., Herring, J. A., et al. (1992). Chemical composition of emissions from the Kuwaiti oil fires. *Journal of Geophysical Research*, 97(14), 483–14489.

Ferraro, G., Baschek, B., de Montpellier, G., et al. (2010). On the SAR derived alert in the detection of oil spills according to the analysis of the EGEMP. *Marine Pollution Bulletin*, 60, 91–102.

Fingas, M. (1996). The evaporation of oil spills: Prediction of equations using distillation data. *Spill Science & Technology Bulletin*, 3, 191–192.

Fingas, M. (2011). An overview of in-situ burning. *Oil Spill Science and Technology* (pp. 737–903). Boston: Gulf Professional Publishing.

Fingas, M. F., & Brown, C. E. (1997). Review of oil spill remote sensing. *Spill Science & Technology Bulletin*, 4, 199–208.

Fingas, M., & Brown, C. (2002). Review of oil spill remote sensors. *Seventh international conference on remote sensing for marine and coastal environments*. Miami, Florida: ERIM International.

Fingas, M., & Brown, C. E. (2011). Oil spill remote sensing: A review. *Oil spill science and technology* (pp. 111–169). Boston: Gulf Professional Publishing.

Gade, M., Alpers, W., Hühnerfuss, H., et al. (1998). On the reduction of the radar backscatter by oceanic surface films: Scatterometer measurements and their theoretical interpretation. *Remote Sensing of Environment*, 66, 52–70.

Gade, M., Alpers, W., Hühnerfuss, H., et al. (1998). Imaging of biogenic and anthropogenic ocean surface films by the multifrequency/multipolarization SIR-C/X-SAR. *Journal of Geophysical Research*, 103, 18,851–18,866.

Garcia-Pineda, O., MacDonald, I., Zimmer, B., et al. (2010). Remote-sensing evaluation of geophysical anomaly sites in the outer continental slope, northern Gulf of Mexico. *Deep-Sea Research II*, 57, 1859–1869.

Garcia-Pineda, O., Zimmer, B., Howard, M., et al. (2009). Using SAR images to delineate ocean oil slicks with a texture-classifying neural network algorithm. *Canadian Journal of Remote Sensing*, 35, 411–421.

Giglio, L., Descloitres, J., Justice, C. O., & Kaufman, Y. J. (2003). An enhanced contextual fire detection algorithm for MODIS. *Remote Sensing of Environment*, 87, 273–282.

Green, R. O., Eastwood, M. L., Sarture, C. M., et al. (1998). Imaging spectroscopy and the Airborne Visible/Infrared Imaging Spectrometer (AVIRIS). *Remote Sensing of Environment*, 65, 227–248.

Grierson, I. T. (1998). Use of airborne thermal imagery to detect and monitor inshore oil spill residues during darkness hours. *Environmental Management*, 2, 905–912.

Hackwell, J. A., Warren, D. W., Bongiovio, et al. (1996). LWIR/MWIR imaging hyperspectral sensor for airborne and ground-based remote sensing. *SPIE 2819* (pp. 102–107). Denver, CO: SPIE.

HAZMAT (1996). Aerial observations of oil at sea. NOAA, Hazardous Materials Response and Assessment Division, Report No. 96-7 (pp. 15).

Hengstermann, T., & Reuter, R. (1990). Lidar fluorescensing of mineral oil spills on the sea surface. *Applied Optics*, 29, 3218–3227.

Hensley, S., Zebker, H., Jones, C., et al. (2009). First deformation results using the NASA/JPL UAVSAR instrument. *2nd Asian-Pacific Conference on Synthetic Aperture Radar* (pp. 1051–1055). Xi'an Shanxi, China: IEEE.

Hobbs, P. V., & Radke, L. F. (1992). Airborne studies of the smoke from the Kuwait oil fires. *Science*, 256, 987–991.

Hollinger, J. P., & Mennella, R. A. (1973). Oil spills: Measurements of their distributions and volumes by multifrequency microwave radiometry. *Science*, 181, 54–56.

Holt, B. (2004). SAR imaging of the ocean surface. In C. R. Jackson, & J. R. Apel (Eds.), *Synthetic aperture radar (SAR) marine user's manual* (pp. 25–79). Washington DC: NOAA NESDIS Office of Research and Applications.

Hörig, B., Kühn, F., Oschütz, F., & Lehmann, F. (2001). HyMap hyperspectral remote sensing to detect hydrocarbons. *International Journal of Remote Sensing*, 22, 1413–1422.

Hu, C., Li, X., Pichel, W. G., & Muller-Karger, F. E. (2009). Detection of natural oil slicks in the NW Gulf of Mexico using MODIS imagery. *Geophysical Research Letters*, 36.

Hu, Y., Winkler, D., Vaughan, M., et al. (2009). CALIPSO/CALIOP cloud phase discrimination algorithm. *Journal of Atmospheric and Oceanic Technology*, 26, 2293–1309.

Hühnerfuss, H., Alpers, W., Dannhauer, H., et al. (1996). Natural and man-made sea slicks in the North Sea investigated by a helicopter-borne 5-frequency radar scatterometer. *International Journal of Remote Sensing*, 17, 1567–1582.

Hühnerfuss, H., Alpers, W., Garrett, W. D., et al. (1983). Attenuation of capillary and gravity waves at sea by monomolecular organic surface films. *Journal of Geophysical Research*, 88, 9809–9816.

Husain, T., & Amin, M. B. (1995). Kuwait oil fires: Regional environmental perspectives. (1st ed.). New York: Pergamon.

HyspIRI (2011). *HyspIRI mission study website*. Pasadena: NASA. [www.hyspiri.jpl.nasa.gov](http://www.hyspiri.jpl.nasa.gov). Access: 6 Mar. 2011.

Ivanov, A. Y., & Zatyagalova, V. V. (2008). A GIS approach to mapping oil spills in a marine environment. *International Journal of Remote Sensing*, 29, 6297–6313.

Jensen, J. R., Ramsey, E. W., Holmes, J. M., et al. (1990). Environmental sensitivity index (ESI) mapping for oil spills using remote sensing and geographic information system technology. *International Journal of Geographical Information Systems*, 4, 181–201.

Jernelöv, A. (2010). The threats from oil spills: Now, then, and in the future. *AMBIO: A Journal of the Human Environment*, 39, 353–366.

Jones, B. (2001). A comparison of visual observations of surface oil with Synthetic Aperture Radar imagery of the *Sea Empress* oil spill. *International Journal of Remote Sensing*, 22, 1619–1638.

Jones, C., & Davis, B. (2011). High resolution radar for response and recovery: Monitoring containment booms in Barataria Bay. *Photogrammetric Engineering and Remote Sensing*, 77, 102–105.

Jones, C. E., Minchew, B., Holt, B., Hensley, S., & Hensley, S. (2011). Studies of the Deepwater Horizon oil spill with the UAVSAR radar. In Y. Liu, A. MacFadyen, Z.-G. Ji, & R. H. Weisberg (Eds.), *Monitoring and modeling the Deepwater Horizon oil spill: A record-breaking enterprise*, *Geophysical Monograph Series*, vol. 195. (pp. 33–50) Washington, D.C.: AGU.

Joye, S. B., MacDonald, I. R., Leifer, I., & Asper, V. (2011). Magnitude and oxidation potential of hydrocarbon gases released from the BP oil well blowout. *Nature Geosciences*, 4, 160–164.

Klemas, V., & Polis, D. F. (1977). A study of density fronts and their effects on coastal pollutants. *Remote Sensing of Environment*, 6, 95–126.

Kokaly, R. F., Roberts, D. A., Heckman, D., et al. (2010). Characterizing the impacts of the Deepwater Horizon oil spill on marshland vegetation, Gulf Coast Louisiana, using airborne imaging spectroscopy. *American Geophysical Union Fall Meeting Abstracts*, 2010AGUFM31B07474K.

Kroutil, R. T., Shen, S. S., Lewis, P. E., et al. (2011). Airborne remote sensing for Deepwater Horizon oil spill emergency response. In S. S. Shen, & P. E. Lewis (Eds.), *SPIE*. Orlando, Florida: SPIE pp. 78120E–78121–782120E–782113.

Kühn, F., Oppermann, K., & Hörig, B. (2004). Hydrocarbon Index—An algorithm for hyperspectral detection of hydrocarbons. *International Journal of Remote Sensing*, 25, 2467–2473.

Lammoglia, T., & Filho, C. R. d. S. (2011). Spectroscopic characterization of oils yielded from Brazilian offshore basins: Potential applications of remote sensing. *Remote Sensing of Environment*, 115, 2525–2535.

Lehr, W. J. (2010). Visual observations and the Bonn Agreement. *Thirty-third Arctic and Marine Oil spill Program (AMOP) Technical Seminar* (pp. 669–678). Ottawa, Ontario, Canada: Environment Canada.

Lehr, W. J., Cekirge, H. M., Fraga, R. J., & Belen, M. S. (1984). Empirical studies of the spreading of oil spills. *Oil and Petrochemical Pollution*, 2, 7–11.

Lehr, W. J., & Simecek-Beatty, D. (2000). The relation of Langmuir circulation processes to the standard oil spill spreading, dispersion, and transport algorithms. *Spill Science & Technology Bulletin*, 6, 247–253.

Lehr, B., Sky, B., Possolo, A., et al. (2010). Oil budget calculator Deepwater Horizon: A report to the National Incident Command. : NOAA.

Leifer, I., Luyendyk, B., & Broderick, K. (2006). Tracking an oil slick from multiple natural sources, Coal Oil Point, California. *Marine and Petroleum Geology*, 23, 621–630.

Lennon, M., Babichenko, S., Thomas, N., et al. (2006). Detection and mapping of oil slicks in the sea by combined use of hyperspectral imagery and laser-induced fluorescence. *European Association of Remote Sensing Laboratories* (pp. 120–128). Warsaw, Poland.

Li, L., Ustin, S. L., & Lay, M. (2005). Application of AVIRIS data in detection of oil-induced vegetation stress and cover change at Jornada, New Mexico. *Remote Sensing of Environment*, 94, 1–16.

Limaye, S. S., Ackerman, S. A., Fry, P. M., et al. (1992). Satellite monitoring of smoke from the Kuwait oil fires. *Journal of Geophysical Research*, 97, 14551–14563.

Liu, P., Li, X., Qu, J. J., et al. (2011). Oil spill detection with fully polarimetric UAVSAR data. *Marine Pollution Bulletin*, 62, 2611–2618.

Lu, J., Lim, H., Liew, S. C., et al. (1999). Oil pollution statistics in Southeast Asian waters compiled from ERS SAR imagery. *Earth Observation Quarterly*, 61. (pp. 13–17): ESA Publication EOQ.

Lucke, R. L., Corson, M., McGlothlin, et al. (2011). Hyperspectral imager for the coastal ocean: Instrument description and first images. *Applied Optics*, 50, 1501–1516.

MacDonald, I. R., Leifer, I., Sassen, R., et al. (2002). Transfer of hydrocarbons from natural seeps to the water column and atmosphere. *Geofluids*, 2, 95–107.

Michel, J., & Galt, J. A. (1995). Conditions under which floating slicks can sink in marine settings. *Proceedings of the 1995 International Oil Spill Conference* (pp. 573–576). Long Beach, California: American Petroleum Institute Pub No 4620.

Migliaccio, M., Gambardella, A., Nunziata, F., et al. (2009). The PALSAR polarimetric mode for sea oil slick observation. *IEEE Transactions on Geoscience and Remote Sensing*, 47, 4032–4041.

Minchew, B., Jones, C., & Holt, B. (2012). Polarimetric L-band SAR signatures of oil from the Deepwater Horizon spill. *IEEE Trans. Geoscience Remote Sensing*, <http://dx.doi.org/10.1109/TGRS.2012.2185804>.

MISR (2010). MISR provides unique views of Gulf oil slick. [www-misr.jpl.nasa.gov/multimedia/collectionImagery/?ImagelD=333&Filter=Off&ThemeSort=&TypeSort=%3E](http://www-misr.jpl.nasa.gov/multimedia/collectionImagery/?ImagelD=333&Filter=Off&ThemeSort=&TypeSort=%3E)

NASA (1991). Landsat 5 images of Kuwait burning 1991. [www.nasa.gov/centers/goddard/images/content/93644main\\_kwaiyat.0001copy.tif](http://www.nasa.gov/centers/goddard/images/content/93644main_kwaiyat.0001copy.tif)

NASA (2004). MODIS Terra image of major pipeline oil rupture in S. Iraq, Mar. 23 2004. [eospis.gsfc.nasa.gov/ve/6303/Iraq/A2004086.0755.250m.jpg](http://eospis.gsfc.nasa.gov/ve/6303/Iraq/A2004086.0755.250m.jpg)

NOAA (1991). Multispectral, false color Persian Gulf oil fires NOAA AVHRR (RGB=Ch3,2,1). [www.parstimes.com/spaceimages/fires-kuwait-4.jpg](http://www.parstimes.com/spaceimages/fires-kuwait-4.jpg)

NOAA (2003). MODIS false color image of smoke plumes from burning oil wells. [www.osei.noaa.gov/Events/Iraq/2003/FHSiraoil\\_076\\_MO.jpg](http://osei.noaa.gov/Events/Iraq/2003/FHSiraoil_076_MO.jpg)

NOAA (2010). NOAA buoy station 42872 Mississippi Canyon Deepwater Horizon. [www.ndbc.noaa.gov/station\\_page.php?station=42872](http://www.ndbc.noaa.gov/station_page.php?station=42872)

NOAA (2010). NOAA buoy station 42040 (Luke offshore test platform). [www.ndbc.noaa.gov/station\\_history.php?station=42040](http://www.ndbc.noaa.gov/station_history.php?station=42040)

Nordvik, A. B. (1995). The technology windows-of-opportunity for marine oil spill response as related to oil weathering and operations. *Spill Science & Technology Bulletin*, 2, 17–46.

NRC (2003). *Oil in the sea III: Inputs, fates, and effects* (pp. 265). Washington, D.C.: National Academy of Sciences.

Otremba, Z., & Piskozub, J. (2004). Modelling the bidirectional reflectance distribution function (BRDF) of seawater polluted by an oil film. *Optics Express*, 12, 1671–1676.

Pilon, R. O., & Purves, C. G. (1973). Radar imagery of oil slicks. *IEEE Transactions on Aerospace and Electronics Systems*, AES-9, 630–637.

Ramirez-Marquez, J. E., & Sausier, B. J. (2009). System development planning via system maturity optimization. *IEEE Transactions on Engineering Management*, 56, 533–548.

Ramsey, E., Rangoonwala, A., Suzuki, Y., & Jones, C. E. (2011). Oil detection in a coastal marsh with polarimetric synthetic aperture radar (SAR). *Remote Sensing*, 3, 2630–2662.

Reed, M., Johansen, O., Brandvik, P. J., et al. (1999). Oil spill modeling towards the close of the 20th century: Overview of the state of the art. *Spill Science & Technology Bulletin*, 5, 3–16.

Riazi, M. R., & Al-Enezi, G. A. (1999). Modeling of the rate of oil spill disappearance from seawater for Kuwaiti crude and its products. *Chemical Engineering Journal*, 73, 161–172.

Roberts, D. A., Gardiner, M., Church, R., et al. (1998). Mapping chaparral in the Santa Monica Mountains using multiple endmember spectral mixture models. *Remote Sensing of Environment*, 65, 267–279.

Ross, S., & Buist, I. (1995). Preliminary laboratory study to determine the effect of emulsification on oil spill evaporation. *Proceedings of the 18th Arctic and Marine Oil-spill Program (AMOP) Technical Seminar* (pp. 91–99). Alberta, Canada: Environment Canada.

Ryerson, T. B., Aikin, K., Angevine, W., et al. (2011). Marine spill atmospheric emissions constrain air–water partitioning, hydrocarbon fate, and leak rate. *Geophysical Research Letters*, 38, L07803.

Salisbury, J. W., d'Aria, D. M., & Sabins, F. F., Jr. (1993). Thermal infrared remote sensing of crude oil slicks. *Remote Sensing of Environment*, 45, 225–231.

Shen, S. S., & Lewis, P. E. (2011). Deepwater Horizon oil spill monitoring using airborne multispectral infrared imagery. *SPIE*. Orlando, Florida: SPIE pp. 80480H-80481-80480H-80416.

Shi, L., Ivanov, A., He, M., & Zhao, C. (2008). Oil spill mapping in the western part of the East China Sea using synthetic aperture radar imagery. *International Journal of Remote Sensing*, 29, 6315–6329.

Singh, K. P., Gray, A. L., Hawkins, R. K., & O'Neil, R. A. (1986). The influence of surface oil on C- and Ku-band ocean backscatter. *IEEE Transactions on Geoscience and Remote Sensing*, GE-24, 738–744.

Solberg, A. H. S., Storvik, G., Solberg, R., & Volden, E. (1999). Automatic detection of oil spills in ERS SAR images. *IEEE Transactions on Geoscience and Remote Sensing*, 37, 1916–1924.

Svejkovsky, J. (2009). *Development of a portable multispectral aerial sensor for real-time oil spill thickness mapping in coastal and offshore waters* (pp. 32). U.S. Minerals Management Service.

Svejkovsky, J., Muskat, J., & Mullin, J. (2009). Adding a multispectral aerial system to the oil spill response arsenal. *Sea Technology*, 50, 17–22.

Swayze, G. A., Furlong, E. T., & Livo, K. E. (2007). Mapping pollution plumes in areas impacted by Hurricane Katrina with imaging spectroscopy. *American Geophysical Union, Fall Meeting, Abstract* (pp. H31L-07). San Francisco: American Geophysical Union.

Taft, D. G., Egging, D. E., & Kuhn, H. A. (1995). Sheen surveillance: An environmental monitoring program subsequent to the 1989 Exxon Valdez shoreline cleanup. In P. G. Wells, J. N. Butler, & J. S. Hughes (Eds.), *Exxon Valdez oil spill: Fate and effects in Alaskan waters, ASTM STP 1219* (pp. 215–238). Philadelphia: American Society for Testing and Materials.

Thorpe, S. A. (1995). Dynamical processes of transfer at the sea surface. *Progress in Oceanography*, 35, 315–352.

Topouzelis, K., Karathanassi, V., Pavlakis, P., & Rokos, D. (2007). Detection and discrimination between oil spills and look-alike phenomena through neural networks. *ISPRS Journal of Photogrammetry and Remote Sensing*, 62, 264–270.

Trivero, P., & Biamino, W. (2010). Observing marine pollution with Synthetic Aperture Radar. In P. Importore, & D. Riccio (Eds.), *Geoscience and remote sensing new achievements* (pp. 397–418). In Tech.

Tseng, W. Y., & Chiu, L. S. (1994). AVHRR observations of Persian Gulf oil spills. *Geoscience and remote sensing symposium. IGARSS '94. Surface and atmospheric remote sensing: Technologies, data analysis and interpretation* (pp. 779–782).

Ud Din, S., Al Dousari, A., & Literathy, P. (2008). Evidence of hydrocarbon contamination from the Burgan oil field, Kuwait—Interpretations from thermal remote sensing data. *Journal of Environmental Management*, 86, 605–615.

van der Meijde, M., van der Werff, H. M. A., Jansma, P. F., et al. (2009). A spectral-geophysical approach for detecting pipeline leakage. *International Journal of Applied Earth Observation and Geoinformation*, 11, 77–82.

Washburn, L., Clark, J. F., & Kyriakidis, P. (2005). The spatial scales, distribution, and intensity of natural marine hydrocarbon seeps near Coal Oil Point, California. *Marine and Petroleum Geology*, 22, 569–578.

Wettle, M., Daniel, P. J., Logan, G. A., & Thankappan, M. (2009). Assessing the effect of hydrocarbon oil type and thickness on a remote sensing signal: A sensitivity study based on the optical properties of two different oil types and the HYMAP and Quickbird sensors. *Remote Sensing of Environment*, 113, 2000–2010.

Wismann, V., Gade, M., Alpers, W., & Hühnerfuss, H. (1998). Radar signatures of marine mineral spills measured by an airborne multi-frequency radar. *International Journal of Remote Sensing*, 19, 3607–3623.

Yoshioka, G., Wong, E., Grossman, B., et al. (1999). Past in situ burning possibilities. *Spill Science & Technology Bulletin*, 5, 349–351.

Young, S. J., Johnson, B. R., & Hackwell, J. A. (2002). An in-scene method for atmospheric compensation of thermal hyperspectral data. *Journal of Geophysical Research*, 107, 4774–4794.